IOP Publishing and International Atomic Energy Agency Nuclear Fusion
Nucl. Fusion **52** (2012) 054003 (16pp) doi:10.1088/0029-5515/52/5/054003

Screening of resonant magnetic perturbations by flows in tokamaks

M. Becoulet[1], F. Orain[1,2], P. Maget[1], N. Mellet[1], X. Garbet[1], E. Nardon[1], G.T.A. Huysmans[3], T. Casper[3], A. Loarte[3], P. Cahyna[4], A.Smolyakov[5], F.L. Waelbroeck[6], M. Schaffer[7], T. Evans[7], Y. Liang[8], O. Schmitz[8], M. Beurskens[9], V. Rozhansky[10] and E. Kaveeva[10]

[1] CEA/IRFM Cadarache, F-13108, St. Paul-lez-Durance, France
[2] PHELMA, Grenoble INP, Minatec, 3 Parvis Louis Néel, BP 257, 38016 Grenoble, France
[3] ITER Organization, Route de Vinon, CS 90046, 13067 Saint Paul lez Durance Cedex, France
[4] Institute of Plasma Physics AS CR v.v.i., Association EURATOM/IPP.CR, Prague, Czech Republic
[5] Physics and Engineering Physics Department, University of Saskatchewan, 116 Science Place, Saskatoon, SK S7N 5E2, Canada
[6] Institute for Fusion Studies, University of Texas, Austin, TX 78712, USA
[7] General Atomics, PO Box 85608, San Diego, CA 92186-5688, USA
[8] Association EURATOM-Forschungszentrum Jülich GmbH, D-52425 Jülich, Germany
[9] Euratom-UKAEA Fusion Association, Culham Science Centre, Abingdon OX113 3EA, UK
[10] St Petersburg State Polytechnical University, Polytechnicheskaya 29, 195251 St Petersburg, Russia

Received 17 June 2011, accepted for publication 19 October 2011
Published 9 May 2012
Online at stacks.iop.org/NF/52/054003

Abstract
The non-linear reduced four-field RMHD model in cylindrical geometry was extended to include plasma rotation, neoclassical poloidal viscosity and two fluid diamagnetic effects. Interaction of the static resonant magnetic perturbations (RMPs) with the rotating plasmas in tokamaks was studied. The self-consistent evolution of equilibrium electric field due to RMP penetration is taken into account in the model. It is demonstrated that in the pedestal region with steep pressure gradients, mean flows perpendicular to the magnetic field, which includes $\vec{E} \times \vec{B}$ and electron diamagnetic components plays an essential role in RMP screening by plasma. Generally, the screening effect increases for lower resistivity, stronger rotation and smaller RMP amplitude. Strong screening of central islands was observed limiting RMP penetration to the narrow region near the separatrix. However, at certain plasma parameters and due to the non-linear evolution of the radial electric field produced by RMPs, the $\vec{E} \times \vec{B}$ rotation can be compensated by electron diamagnetic rotation locally. In this case, RMPs can penetrate and form magnetic islands. Typical plasma parameters and RMPs spectra on DIII-D, JET and ITER were used in modelling examples presented in the paper.

(Some figures may appear in colour only in the online journal)

1. Introduction

Type I ELMs represent a particular danger for plasma-facing components (PFCs) and divertor materials in ITER due to the fast (~0.25 ms) transient release of energy (up to 20 MJ) in ELM crash [1–3]. The promising active method of ELM control by resonant magnetic perturbations (RMPs) produced by specific coils permitted total type I ELM suppression on DIII-D [4, 5] and AUG [6] or strong mitigation of the ELM size [7] on JET. However, at present, the underlying physics of ELM suppression is not totally understood up to the point to give reliable predictions for type I ELM suppression by RMPs in ITER. As shown in DIII-D experiments, ELMs are essentially suppressed if according to the vacuum modelling magnetic islands overlap (Chirikov parameter >1), creating an ergodic region at the plasma edge for $r/a > 0.9$ [8]. The present RMP system foreseen for ITER was essentially designed on this semi-empirical and 'vacuum' without plasma response modelling background [9, 10]. However, present day RMP experiments demonstrated already that 'vacuum' criterion [8] is not sufficient. At similar to DIII-D *a priori* 'vacuum' edge ergodization [8], the application of RMPs demonstrated a

variety of ELM responses on different machines. In particular, ELM suppression on DIII-D [4, 5, 11] and on AUG [6] was observed, ELM mitigation was demonstrated on JET [7], type III ELM triggering is seen in ELM free discharges on NSTX [12], triggering small type IV ELMs are typical for MAST [13]. Moreover, the ELM reaction on RMPs for a single machine depends on equilibrium, plasma parameters and RMP spectrum. Unfortunately, the direct measurement of static RMPs in plasma is not developed yet and one can conclude only indirectly if RMP penetrates or not observe, for example, characteristic features as density 'pump-out', toroidal rotation braking, strike points splitting, ELM mitigation, etc [4–13]. The present lack of understanding of plasma response to RMPs represents an issue for reliable extrapolations of the RMP method to ITER. In this respect, non-linear MHD theory and modelling can provide further physical and numerical improvements to refine knowledge of basic ELM dynamics and related ELM control techniques [14]. The present studies of plasma response to static RMPs based on non-linear MHD theory and modelling [15–22] are still in the initial stage and far from a self-consistent complete picture, but they demonstrated already the particularly important role of plasma flows with respect to RMP penetration into the plasma. Depending on the plasma parameters and RMP spectrum, the actual RMP field could be very different in rotating plasmas where the generation of current perturbations on the rational surfaces could prevent reconnections and island formation, leading to the effective screening of RMPs [15–20]. The equilibrium radial electric field produces $\vec{E} \times \vec{B}$ rotation which, together with the diamagnetic electron rotation, is particularly important in the RMPs screening in the pedestal region [22, 23]. In this work, the resistive MHD rotating plasma response to RMPs is studied using a non-linear code RMHD [24, 25]. The RMHD code [24] is adapted to RMP studies in [17, 22] and further developed in this paper to include neoclassical poloidal viscosity tensor and two fluid diamagnetic effects, neglected in the previous RMP modelling [17]. In this work, we introduced this new physics in order to describe self-consistently the evolution of the equilibrium radial electric field and the rotation perpendicular to the magnetic field due to RMP penetration in the pedestal region. This is the essential new step forward compared with [17, 22], where equilibrium electric field was taken from the experiment [5] and kept constant in the modelling [22]. Generally in experiments of type I ELM suppression by RMPs on DIII-D the radial electric field in the pedestal tends to more positive values at the edge with the minimum of the 'well' shifted towards the core [5]. In the model we use in this work, this trend in the changes in the equilibrium electric field due to RMPs can be reproduced.

The paper is organized as follows. In section 2 the derivation of the numerical non-linear RMHD model with diamagnetic and neoclassical effects is described. Section 3 is devoted to the description of the generic features of the single RMP harmonic and RMP spectrum penetration into the plasma with flows. In this section DIII-D-like parameters are used. In section 4 more realistic equilibrium, plasma parameters and error field correction coil (EFCC) spectra for toroidal number $n = 2$ are used in the modelling of RMP screening in JET. In section 5 modelling results of rotating plasma interaction with RMPs are presented for the standard H-mode scenario and actual design of in-vessel RMP coils in ITER.

2. Model

2.1. Four-field reduced MHD model with neoclassical poloidal viscosity

The well known four-field non-linear reduced resistive RMHD model [24–26] was used as a starting set of the equations. The normalized, as in [17], system of non-linear RMHD equations with diamagnetic and neoclassical effects was solved in the following form:

$$\frac{\partial \psi}{\partial t} = -\eta(J - J_{t=0}) - \nabla_{\parallel}(\Phi - \delta p) \tag{2.1}$$

$$\frac{\partial W}{\partial t} + V\nabla_{\parallel} W = [W, \Phi + \tau\delta p] - \nabla_{\parallel} J + \tau\delta[\nabla_{\perp} p, \nabla_{\perp}\Phi] + F^{\text{neo}}_{\perp,0,0} + \nu_{\perp}\nabla^2 W \tag{2.2}$$

$$\frac{\partial p}{\partial t} + V\nabla_{\parallel} p = [p, \Phi] + k_{\perp}\nabla^2 p + S_p \tag{2.3}$$

$$\frac{\partial V}{\partial t} + V\nabla_{||} V = [V, \Phi] - \frac{1+\tau}{2}\nabla_{\parallel} p + F^{\text{neo}}_{||,0,0} + \nu_{\parallel}\nabla^2 V + S_V. \tag{2.4}$$

Compared with [24] we neglected small electron inertia and finite β-terms. Here normalized variables are ψ the poloidal flux, p the electron pressure, Φ the electrostatic potential, ion velocity parallel to the total magnetic field $\vec{B}$ is $\vec{V}_{||,\text{i}} = (1/B^2)(\vec{V}_{\text{i}}\vec{B})\vec{B} = V\vec{b}$,

$$J = -\nabla^2_{\perp}\psi = -\left(\frac{1}{r}\frac{\partial}{\partial r}\left(r\frac{\partial \psi}{\partial r}\right) + \frac{1}{r^2}\frac{\partial^2 \psi}{\partial^2 \theta}\right)$$

is the parallel current, $W = -\nabla^2_{\perp}\Phi$ the vorticity, dimensionless parameter $\delta = 1/2\Omega_{\text{ci}}\tau_{\text{A}}$, where $\Omega_{\text{ci}} = eB_{\text{T}}/m_{\text{i}}$ is ion gyrofrequency, Alfvén velocity $V_{\text{A}} = B_{\text{T}}/\sqrt{\mu_0 m_{\text{i}} n_0}$, electron density $n_{\text{e}} = Zn_{\text{i}}$; $Z = 1$. Ion $T_{\text{i}}(r)$ and electron $T_{\text{e}}(r)$ temperature profiles are fixed, and $T_{\text{i}}(r)/T_{\text{e}}(r) = \tau = \text{const}$. Total pressure $P = P_{\text{i}} + P_{\text{e}} = p(1+\tau)$ is evolving only due to the electron density transport. The diffusion coefficient in (2.3) $k_{\perp} \sim 10^{-5}$–10^{-6}corresponding to typical experimental values due to turbulent transport was constant in modelling. Parallel viscosity coefficient in (2.4) represents phenomenological parallel viscosity due to the turbulence. Typical experimental value was used: $\nu_{||} \sim 10^{-6}$. Cylindrical coordinates $\{r; \theta; z\}$ were used in the code. Here $z \approx R_0\varphi$. φ is the toroidal angle, θ is the poloidal one, $R_0 = R_M/a$ is the normalized major radius. The magnetic field normalized to the value on the axis (B_0) is represented in cylindrical approximation as

$$\vec{B}/B_0 \approx (\vec{e}_z + \nabla\psi \times \vec{e}_z) = \left(\frac{1}{r}\frac{\partial \psi}{\partial \theta}; -\frac{\partial \psi}{\partial r}; 1\right).$$

Equilibrium magnetic field is

$$\vec{B}_{\text{eq}} \approx B_0(0, b_{\theta,0}(r), b_{z,0}); \qquad b_{z,0} = 1;$$
$$b_{\theta,0}(r) = -\frac{\partial \psi_0}{\partial r} = \frac{r}{qR_0}.$$

Note that in this approximation both equilibrium and perturbed magnetic fields are divergence free: $\vec{\nabla}\cdot\vec{B} = 0$. For any scalar function S we introduce parallel gradient operator:

$$\nabla_{\parallel} S \equiv \frac{1}{B}\vec{B}\cdot\vec{\nabla}S \approx \frac{\partial S}{\partial z} + \nabla\psi \times \vec{e}_z \cdot \vec{\nabla}S = \frac{\partial S}{\partial z} + [S, \psi],$$

where

$$[S,\psi]=\frac{1}{r}\left(\frac{\partial S}{\partial r}\frac{\partial \psi}{\partial \theta}-\frac{\partial \psi}{\partial r}\frac{\partial S}{\partial \theta}\right) \quad \text{and}$$

$$[\nabla_\perp a,\nabla_\perp b]\equiv\left[\frac{\partial a}{\partial r},\frac{\partial b}{\partial r}\right]+\left[\frac{1}{r}\frac{\partial a}{\partial \theta},\frac{1}{r}\frac{\partial b}{\partial \theta}\right].$$

Resistivity profile follows temperature dependence: $\eta(r)\sim\eta_0(T_e(r)/T_e(0))^{-3/2}$ with typical experimental-like central value $\eta_0=10^{-8}$–10^{-9}. Perpendicular viscosity $\nu_\perp=10^{-8}$ was added for numerical stability reasons in (2.2). Note, however, that typically neoclassical viscosity is much larger $\mu_i/\nu_\perp\sim 10^3$–10^4 (see section 2). Diffusion terms are compensated by volume source terms adjusted to keep initial profile pressure, current and toroidal velocity profile without RMPs. $S_p=-k_\perp\nabla^2 p_{t=0}$; $S_V=-\nu_\parallel\nabla^2 V_{t=0}$. This form of sources in the RMHD code permits initial (at $t=0$) pressure and toroidal rotation profiles to be kept in the absence of RMPs without going into the details of heating, particles and rotation sources which is out of interest in this simple cylindrical model. Similar to this in Ohm's law (2.1) the source term $\eta J_{t=0}$ is introduced to keep the current profile stationary close to the initial value, in the absence of RMPs. Similar to [17] the normalization of the variables used here is the following (here (ph) is for 'physical'):

$$B^{ph}=B_{0,z}B\equiv B_0 B;\quad \psi^{ph}/R_M=aB_0\psi;\quad r^{ph}=ar;$$
$$R_0^{ph}\equiv R_M=aR_0;\quad n_e^{ph}=n_0 n_e;\quad \rho_0=Zm_i n_0;$$
$$V^{ph}=V_A V;\quad t^{ph}=\tau_A t;\quad \tau_A=\frac{a}{V_A};$$
$$\Phi^{ph}=\frac{aB_0^2}{\sqrt{\mu_0\rho_0}}\Phi;\quad p^{ph}=\frac{B_0^2}{2\mu_0}p;\quad \eta^{ph}=\frac{aB_0\sqrt{\mu_0}}{\sqrt{\rho_0}}\eta;$$
$$\nu^{ph}_{(\parallel,\perp)}=\frac{a^2}{\tau_A}\nu_{(\parallel,\perp)}.$$

The details of derivation of the initial four-field model are given in [24]. All variables in the RMHD code [17, 25] used here are represented in Fourier series, for example poloidal flux $\psi=\sum_{m,n=\pm\infty}\psi_{nm}e^{im\theta+inz/R_0}$, and the harmonic $n=0, m=0$ represents the value averaged over the magnetic surface. The boundary conditions at $r=1$ are zero for all perturbations except for the magnetic flux harmonic amplitudes, $\psi_{nm}|_{r=1}\approx\psi^{vac}_{nm,sep}$, which are approximated by the vacuum amplitudes calculated in the toroidal geometry using the code ERGOS [9]. Here we take $r\approx\sqrt{\psi_{pol}}$ as the normalized radial coordinate. The neoclassical terms appear if one takes into account the neoclassical poloidal viscosity tensor in the equation of motion [27]. In the present model neoclassical terms were taken into account only for variables averaged over the magnetic surface, hence for harmonic $n=0, m=0$:

$$F^{neo}_{\perp,0,0}=-\mu_{neo,1}\left\{W_{0,0}-\frac{1}{r}\frac{\partial}{\partial r}\right.$$
$$\left.\times\left(r\left(V_{0,0}\frac{r}{qR_0}+\frac{\tau\delta}{n_{0,0}}\frac{\partial p_{0,0}}{\partial r}+k_i\tau\delta\frac{\partial T_e(r)}{\partial r}\right)\right)\right\} \quad (2.5)$$

$$F^{neo}_{\parallel,0,0}=-\mu_{neo,2}$$
$$\times\left(\frac{\partial\Phi_{0,0}}{\partial r}+V_{0,0}\frac{r}{qR_0}+\frac{\delta\tau}{n_{0,0}}\frac{\partial p_{0,0}}{\partial r}+\tau\delta k_i\frac{\partial T_e(r)}{\partial r}\right) \quad (2.6)$$

where

$$\mu_{neo,1}=\mu_i\left(\frac{qR_0}{r}\right)^2,\quad \mu_{neo,2}=\mu_i\frac{qR_0}{r},$$

$$W_{0,0}=-\nabla^2\Phi_{0,0}=-\frac{1}{r}\frac{\partial}{\partial r}\left(r\frac{\partial\Phi_{0,0}}{\partial r}\right),\quad n_{0,0}=\frac{p_{0,0}}{T_e(r)}.$$

$\mu_i(r)$ the neoclassical poloidal flow damping rate and coefficient $k_i(r)$ are calculated for given plasma parameters using formulae from [27, 28]. The detailed derivation of terms (1.5) and (1.6) is given in the appendix. Note that in the present model without RMPs the poloidal velocity tends to the neoclassical value [27–37]:

$$\frac{\partial\Phi_{0,0}}{\partial r}+V_{0,0}b_\theta+\frac{\delta\tau}{n_{0,0}}\frac{\partial p_{0,0}}{\partial r}+\delta\tau k_i\frac{\partial T_e}{\partial r}=0. \quad (2.7)$$

This corresponds for the physical values to

$$\frac{1}{B_T}\frac{\partial\Phi}{\partial r}+V\frac{r}{qR_0}+\frac{1}{m_i n_e\Omega_{ci}}\frac{\partial p_i}{\partial r}+k_i\frac{1}{m_i\Omega_{ci}}\frac{\partial T_i}{\partial r}=0 \quad (2.8)$$

which is equivalent to the force balance equation for the radial electric field:

$$E_r\equiv-\frac{\partial\Phi}{\partial r}\approx\frac{1}{en_e}\frac{\partial p_i}{\partial r}+(V_\varphi B_\theta-V_\theta^{neo}B_\varphi). \quad (2.9)$$

Here in the cylindrical large aspect ratio approximation $V_\varphi\sim V$; $B_\varphi\sim B_0=$ const. In the presence of RMPs radial electric field and poloidal rotation are modified and deviate from the neoclassical value.

2.2. Role of the rotation perpendicular to the magnetic field in screening of RMPs

It is demonstrated theoretically [15, 38] and numerically [16–23] that the plasma response to RMPs mainly consists in generation of current perturbations localized near the rational surfaces, leading to the deformation of the magnetic perturbation compared with the vacuum case. As analysed in [15, 38], depending on the plasma parameters (viscosity, resistivity, rotation, current profiles, etc), the plasma response can vary between stronger or less strong screening, or in some cases amplification of the externally applied static magnetic perturbations. It will be useful for the following discussion of the modelling results to analyse single harmonic perturbation penetration into the rotating plasma. Magnetic flux, current and electron pressure, correspondingly, are represented in the RMHD code as follows: $\psi=\psi_{0,0}(r)+\psi_{nm}(r)e^{im\theta+inz/R_0}+$ cc; $J=J_{0,0}(r)+J_{nm}(r)e^{im\theta+inz/R_0}+$ cc; $p(r)=p_{0,0}(r)+p_{nm}e^{im\theta+inz/R_0}+$ cc. For the equilibrium values: $\nabla_\parallel(\Phi_{0,0}-\delta p_{0,0})=0$, $b_\theta=-(\partial\psi_{0,0}/\partial r)=r/qR_0$. Considering that $J_{0,0}(r)\sim J_{0,0}(t=0)$, the linearized Ohm law (1.10) for a single harmonic perturbation amplitude under stationary conditions can be written as follows:

$$\eta J_{nm}=-\frac{i}{R_0}(\Phi_{nm}-\delta p_{nm})\left(n+\frac{m}{q}\right)$$
$$-\frac{im\psi_{nm}}{r}\frac{\partial(\Phi_{0,0}-\delta p_{0,0})}{\partial r}. \quad (2.10)$$

At the rational surface $q=-m/n$ ($n<0, m>0$ according to the convention used in the RMHD code [25]) and hence

$$\eta J_{nm}=-\frac{im\psi_{nm}}{r}\frac{\partial(\Phi_{0,0}-\delta p_{0,0})}{\partial r}\approx-\frac{im\psi_{nm}}{r}(V_{E,\theta}+V^*_{e,\theta})$$
$$=-b^r_{nm}(V_{E,\theta}+V^*_{e,\theta}). \quad (2.11)$$

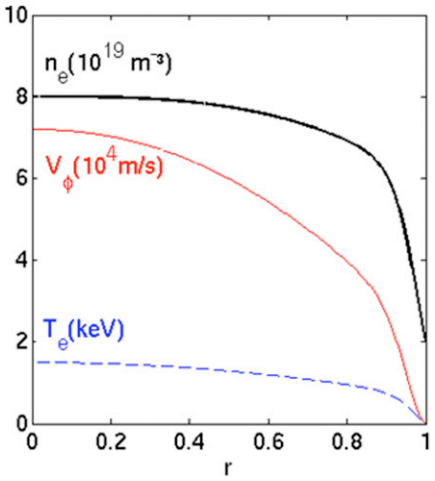

Figure 1. DIII-D-like plasma parameters used in modelling.

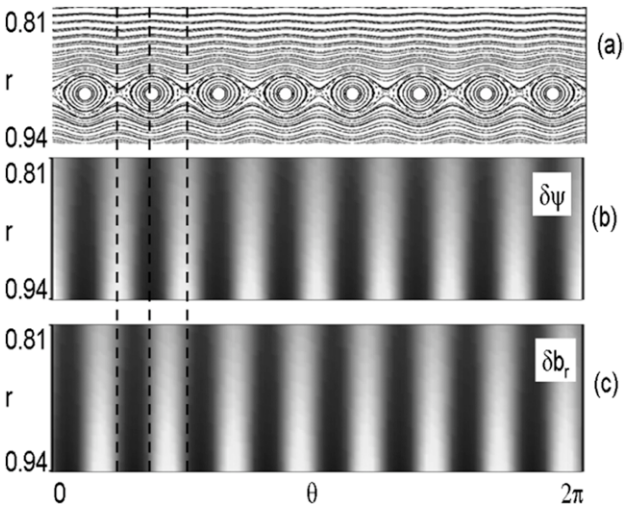

Figure 2. (*a*) Poincaré plot for vacuum-like island on resonant surface $q = 8/3$; (*b*) corresponding to (*a*) magnetic flux perturbation as a function of radial and poloidal coordinates at $z = 0$; (*c*) corresponding to (*a*) radial magnetic field perturbation.

In cylindrical approximation, the normalized perpendicular drift and electron diamagnetic velocities are

$$\vec{V}_E = \left(-\frac{1}{r}\frac{\partial \Phi}{\partial \theta}; \frac{\partial \Phi}{\partial r}; 0\right) \quad \text{and}$$

$$\vec{V}^*_e = -\delta\left(-\frac{1}{r}\frac{\partial p}{\partial \theta}; \frac{\partial p}{\partial r}; 0\right).$$

The current perturbation is zero on the rational surface if $(V_{E,\theta} + V^*_{e,\theta}) \sim 0$, meaning that with respect to the static RMP imposed from the external coils electrons are at rest, and therefore no screening of RMPs is expected for this particular harmonic in this region.

3. Generic features of the single RMP penetration into the plasma with flows

In this section DIIII-D-like parameters [4] were used for modelling: $R_M = 1.8\,\mathrm{m}$, $a = 0.6\,\mathrm{m}$; $B_\varphi \sim B_0 = 1.9\,\mathrm{T}$, cylindrical $q_{95} \sim 3.15$. Plasma parameter profiles used

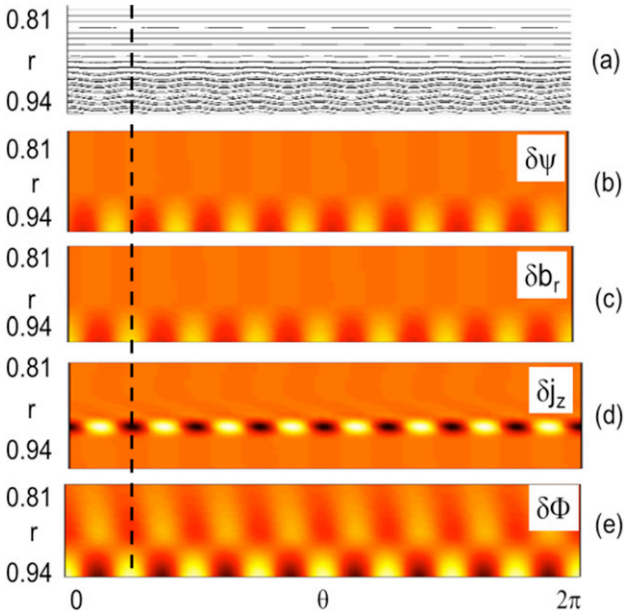

Figure 3. (*a*) Poincaré plot for (8/3) island with plasma response at $q_{95} = 3.15$; $t = 10^5 \tau_A$. (*b*) Magnetic flux perturbation; (*c*) radial magnetic field; (*d*) toroidal current perturbation and (*e*) electrostatic potential perturbation at $z = 0$.

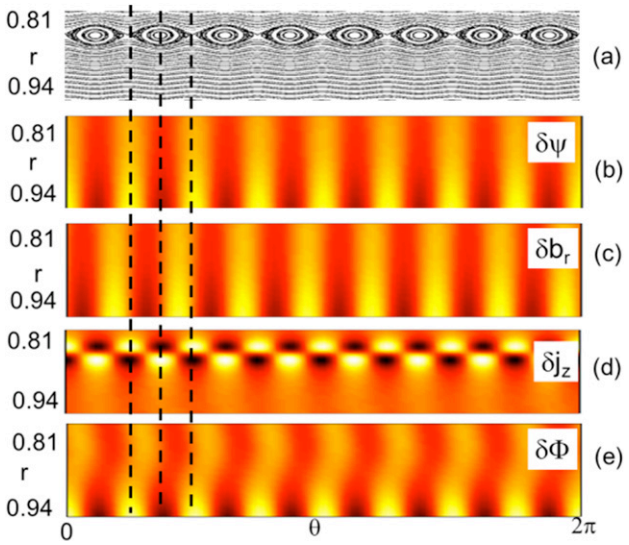

Figure 4. (*a*) Poincaré plot for (8/3) island with plasma response at $q_{95} = 3.44$, $t = 10^5 \tau_A$; (*b*) magnetic flux perturbation; (*c*) radial magnetic field; (*d*) toroidal current perturbation and (*e*) electrostatic potential perturbation at $z = 0$.

in modelling are presented in figure 1. Central density, temperature, toroidal rotation, correspondingly, were $n_{e,0} = 8 \times 10^{19}\,\mathrm{m}^{-3}$; $T_{e,0} = 1.5\,\mathrm{keV}$, $V_0 = 72\,\mathrm{km\,s}^{-1}$. These plasma parameters correspond typically to the high-collisionality regime [4, 5], note, however, that no specific DIII-D shots were modelled here, that is why we call it here the 'DIII-D-like' case. Density, rotation and temperature profiles are approximated here by cubic polynomials multiplied by a factor $f(r) = 0.5(1 - \tanh((r - r_{bar})/\sigma)$ with $r_{bar} = 0.98$, and pedestal width $\sim \sigma = 0.06$. Resistivity profile follows dependence: $\eta(r) \sim \eta_0 (T_e(r)/T_e(0))^{-3/2}$ with a typical experimental-like central value $\eta_0 = 10^{-8}$. Parallel viscosity is $\nu_{||} = 10^{-6}$.

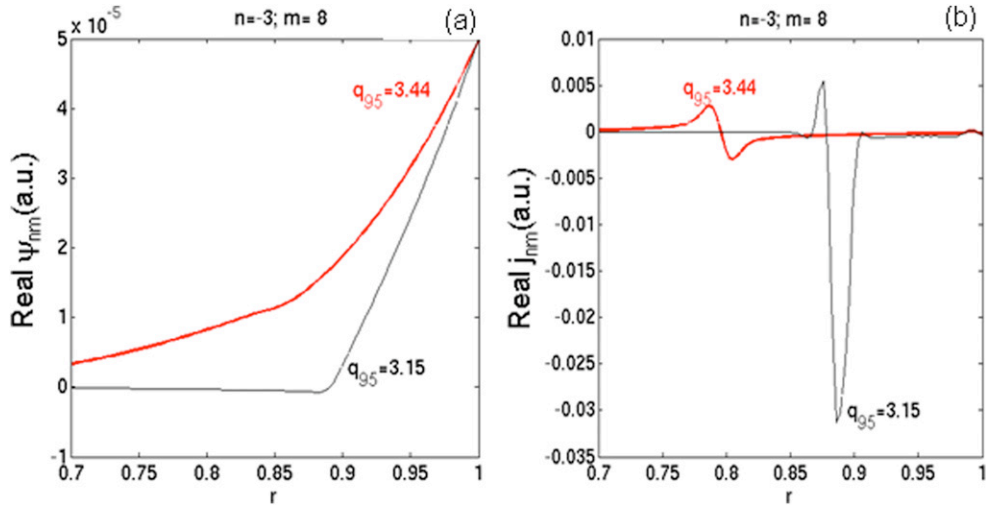

Figure 5. Radial profiles of the magnetic flux perturbation (a) and toroidal current (b) harmonic amplitudes ($n = -3$, $m = 8$) at $q_{95} = 3.15$ (screening of RMP) and $q_{95} = 3.44$ (no screening) under stationary conditions at $t = 10^5 \tau_A$.

Perpendicular numerical viscosity is taken $\nu_\perp = 10^{-8}$, and much larger perpendicular viscosity $\mu_{neo,1,2} \gg \nu_\parallel, \nu_\perp$ is due to the neoclassical mechanism [28]. The exact profiles of $\mu_{neo,1,2}(r)$; $k_i(r)$ for the parameters (figure 1) will be used later on in the paper. For the initial study of the generic features of RMP–plasma interaction, neoclassical coefficients were taken constants: $\mu_{neo,1,2} = 5 \times 10^{-5}$; $k_i = -0.8$. At the boundary, normalized perturbation amplitude was taken $\psi_{nm}(1) \sim 5 \times 10^{-5}$, which was estimated from vacuum modelling with the toroidal vacuum code ERGOS [9] for DIII-D I-coils at 4 kAt, $n = -3$ even parity configuration. As demonstrated in [17], screening of RMPs by plasma is negligible at high resistivity, so we call here a 'vacuum-like' case if RMHD modelling is done at high resistivity: $\eta_0 = 10^{-4}$. The 'vacuum-like' $m = 8, n = -3$ island without neoclassical viscosity and without rotation ($\mu_{neo,1,2} = 0$, $\delta = 0.$ and $V_{\varphi,0} = 0$) is presented in the Poincaré plot in figure 2(a). Corresponding magnetic flux and radial magnetic field perturbation: $\delta\psi(r, \theta, z = 0)$; $\delta b^r(r, \theta, z = 0)$ are presented in figures 2(b) and (c). Note the expected phase shift between $\delta\psi \sim \cos(m\theta)$ and $\delta b^r \sim \sin(m\theta)$, since $\delta b^r = (1/r)(\partial(\delta\psi)/\partial\theta)$. The same kind of plots, but with plasma response with parameters $V_0/V_A \sim 0.022$ (which corresponds to central rotation $\sim$72 km s^{-1}), $\eta_0 = 10^{-8}$, $\delta = 0.03$, $q_{95} = 3.15$, are presented in figure 3 at $t = 10^5 \tau_A$. As shown in [17], the penetration time for RMPs scales approximately as $\sim 1/\eta$, so in the following analysis we present the amplitude of perturbations after $t = 10^4$–$10^5 \tau_A$, when stationary conditions are reached in modelling and the corresponding island has its final size. Note that the current perturbation (figure 3(d)) is localized on the rational surface and is in phase with radial magnetic field perturbation (figure 3(c)) and strong screening of vacuum magnetic perturbation is observed: $\delta b^r|_{r \geqslant r_{res}} \sim 0$. However, for example, at $q_{95} = 3.44$ RMP penetration is seen in modelling (figure 4). In this case the corresponding perturbations have 'vacuum-like' structures and in particular the current perturbation is zero at $r = r_{res}$. The radial profiles of magnetic flux and current perturbation harmonics amplitudes for $q_{95} = 3.15$ and $q_{95} = 3.44$ cases are presented in figure 5. Note that for the parameters used here the screening

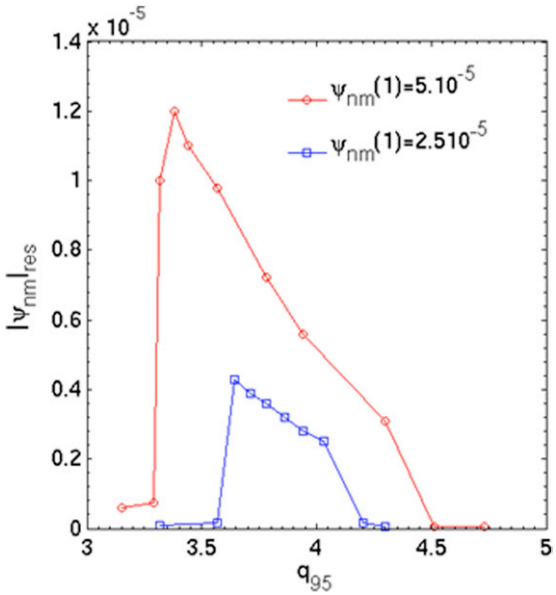

Figure 6. Maximum RMP amplitude on the resonant surface $q = 8/3$ for a single harmonic in q_{95} and RMP edge amplitude scans.

current layer width is about 9 mm. The estimation of the linear layer width according to formula (26) from [15] gave a slightly smaller value $\sim$4 mm compared with modelling. The performed q_{95} scans (figure 6) demonstrated that RMPs penetrate in a window situated around a certain q_{95} for different values of edge RMP amplitude (here for $\psi_{nm}(1) \sim 5 \times 10^{-5}$ and $\psi_{nm}(1) \sim 2.5 \times 10^{-5}$). The decrease in the absolute value of RMP amplitude at the resonance for higher q_{95} values seen in figure 6 is explained by the radial dependence $\psi_{nm}(r) \sim r^m$ in vacuum. The resonant surface $q_{res} = 8/3$ moves towards the plasma centre when q_{95} increases leading to a smaller 'vacuum' island. In figure 6, the RMP penetration window Δq_{95} for the (8/3)-island is $\Delta q_{95} = 1 - 0.5$ (smaller corresponds to smaller RMP amplitude). The reason for no RMP screening seen at $q_{95} = 3.44$ is that $(V_{E,\theta} + V^*_{e,\theta}) \sim 0$ at the resonance surface $q = 8/3$ (figure 7(a)). In contrast $(V_{E,\theta} + V^*_{e,\theta}) \neq 0$ for $q_{95} = 3.15$ (figure 7(b)), so screening currents are not zero

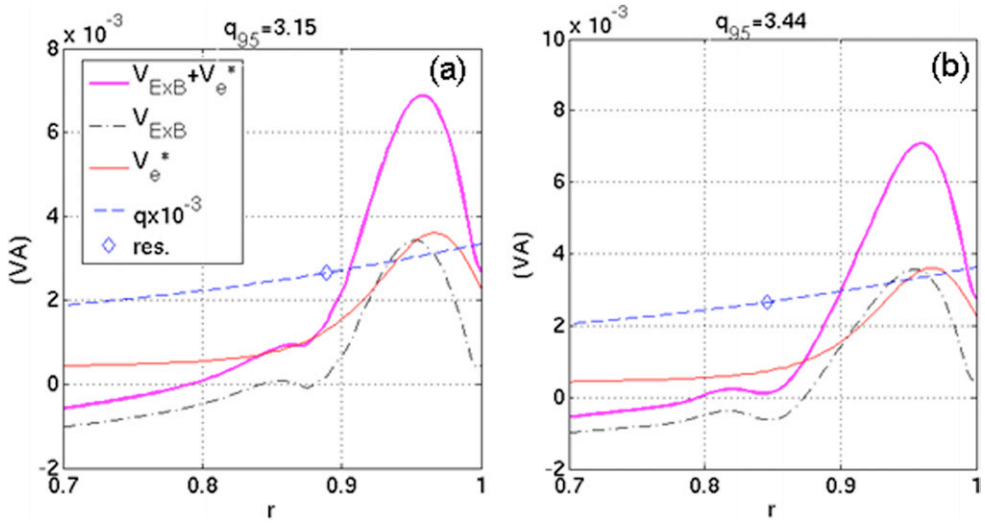

Figure 7. Components of the perpendicular (or 'poloidal' in reduced MHD formulation) velocity: $V_{E,\theta}$ (dashed–dotted line); electron diamagnetic $V^*_{e,\theta}$ (thin); the sum $(V_{E,\theta} + V^*_{e,\theta})$(bold), $q \cdot 10^{-3}$ profile (dashed). The position of $q = 8/3$ resonance is indicated by a diamond for the case of screened island at $q_{95} = 3.15$ (a) and no screening at $q_{95} = 3.44$ (b).

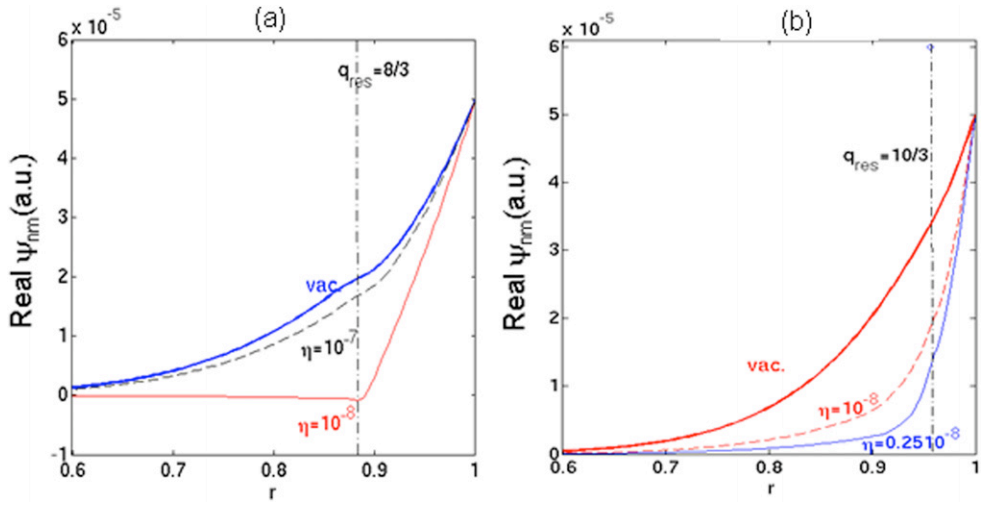

Figure 8. (a) Radial profiles of the magnetic flux perturbation harmonic amplitudes $(n = -3, m = 8)$ at $q_{95} = 3.15$ for different resistivities. (b) The same as (a) for more external island $(n = -3, m = 10)$.

at the rational surface (see the discussion in section 2.2). As already discussed in [15, 17], at higher resistivity, screening currents are small even at non-zero perpendicular rotation and RMP can penetrate. To illustrate this, the radial profiles of the magnetic flux perturbation harmonics are presented for different resistivities in figure 8(a) for the $q_{95} = 3.15$ case. One can see the strong screening of the perturbation for $r > r_{\rm res}$ at $\eta_0 = 10^{-8}$ and the much smaller effect of plasma on RMP at $\eta_0 = 10^{-7}$ compared with a 'vacuum-like' case which corresponds in this modelling to a resistivity $\eta_0 = 10^{-2}$. Since resistivity increases towards the edge due to the temperature dependence, edge islands are typically less screened as illustrated in figure 8(b). The penetration time for RMP increases for lower resistivity (figure 9) [17]. The neoclassical viscosity $\mu_{\rm neo,1,2} = \mu = {\rm const}$ (constant here) scan is presented in figure 10(a), where maximum amplitude of a single harmonic on the resonant surface $q = 8/3$ is presented for different q_{95} values. One can see that at larger viscosity μ the penetration window in terms of Δq_{95} is narrower. In the case of larger neoclassical poloidal viscosity, the initial radial electric field (and hence $\vec{E} \times \vec{B}$ velocity) is less influenced by RMP. This is illustrated in figure 10(b) where the electric field profiles are presented for different values of $\mu_{\rm neo,1,2}$. Magnetic topologies resulting from the application of RMP spectrum $\psi_{n=-3;m=6,7,\ldots,10}(1) = (8; 7; \ldots 4) \times 10^{-5}$ at $q_{95} = 3.15$ in vacuum and with plasma response (under stationary conditions at $t = 6 \times 10^4$) are shown in figure 11. Note the strong screening of more central magnetic islands except on $q = 7/3$. Screening factor $S_{nm} = |\psi^{\rm pl}_{nm}|/|\psi^{\rm vac}_{nm}|$ profile is presented for different values of resistivity $(\eta_0 = 10^{-8}; 2 \times 10^{-8}; 8 \times 10^{-8})$ as a function of poloidal m-number in figure 12. The condition for perpendicular velocity $(V_{E,\theta} + V^*_{e,\theta}) \sim 0$ (figure 13) is satisfied for the island (7/3) for all resistivities which explains why it is not screened. Island $q = (8/3)$ is screened since it is situated at the maximum of the perpendicular velocity in all cases (figure 13). In contrast, more central island on $q = (6/3)$ forms for higher resistivity values: $\eta_0 = 2 \times 10^{-8}; 8 \times 10^{-8}$.

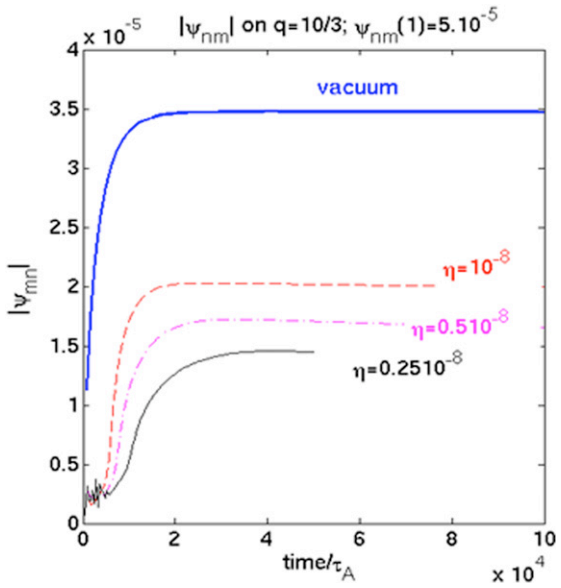

Figure 9. Absolute value of ($n = -3$, $m = 10$) harmonic amplitude on the resonant surface as a function of time for different central resistivity values η_0.

The radial electric field E_r structure with RMP spectrum at $t = 6 \times 10^4 \tau_A$ is shown in figure 14 in comparison with the initial equilibrium electric field. One can see that, due to the non-linear interaction of RMPs with plasma, radial electric field is more positive in the ergodic region and the minimum of the E_r 'well' moves inside the plasma (figure 14), which reminds us of the experimental trend [5].

The realistic neoclassical coefficients (figure 15), calculated for profiles presented in figure 1 according to [28] instead of constants, do not change the generic features of RMP interaction with plasma described above. In particular, RMP screening by plasma is stronger for larger rotation (including diamagnetic), smaller RMP amplitude, smaller resistivity and larger viscosity. However, because of the increase in $\mu_{\mathrm{neo},1,2}$ towards the edge (figure 15), a smaller penetration window $\Delta q_{95} \sim 0.3$ (compared with figure 6 where $\Delta q_{95} \sim 1$) is observed for a single island (8/3) (figure 16). However, edge resonant harmonics still penetrate (figure 17), since typically, the screening currents are smaller at higher resistivity.

4. RMP penetration on JET

In ELM mitigation experiments on JET, RMPs are generated by the external one-row EFCC coils [7] in $n = 1, n = 2$ configurations. Here we present an example of RMHD modelling of plasma response in the shot JET#77329 with parameters $R_M = 2.9\,\mathrm{m}$, $a = 0.89\,\mathrm{m}$, $B_\varphi \sim B_\mathrm{T} = 1.8\,\mathrm{T}$, toroidal rotation in the plasma centre $\Omega_{\varphi,0} = 38.6\,\mathrm{krad\,s^{-1}}$, the parameter in the diamagnetic terms was $\delta = 0.029$, cylindrical $q_{95} \sim 3.8$, EFCC current amplitude $I_{\mathrm{EFCC}} = 40\,\mathrm{kAt}$, $n = -2$. The realistic plasma parameters used in modelling are shown in figure 18. The corresponding normalized neoclassical viscosity coefficients calculated using expressions from [28] are presented in figure 19. The results of vacuum modelling by the ERGOS code [9] in toroidal geometry and equilibrium for the shot JET#77329 are presented in figure 20. At $I_{\mathrm{EFCC}} = 40\,\mathrm{kAt}$ magnetic islands do not overlap even in vacuum modelling (figure 20(*b*)). The normalized absolute values of the magnetic flux perturbation harmonic amplitudes as a function of radius ($r \approx \sqrt{\psi_{\mathrm{pol}}}$) are presented in figure 21. The maximum values of corresponding harmonics amplitudes are used in the cylindrical RMHD code as boundary conditions: $\psi_{n=-2;m=3,4,..8}(1) = (9.9; 6.5; 4.4; 2.9; 2; 1.4;) \times 10^{-5}$. The perpendicular rotation profile with respect to the position of the resonances is a crucial factor in RMP screening by plasma. However, in order to have the same q-profile in the cylindrical code as in toroidal geometry $q = q_{\mathrm{tor}}$, it is necessary to adapt equilibrium poloidal field and current profile in the RMHD code accordingly and in particular

$$B_\theta = \frac{r B_0}{R_0 q_{\mathrm{tor}}}; \qquad j_z = \frac{1}{\mu_0}\vec{e}_z(\nabla \times \vec{B}) = \frac{1}{\mu_0}\frac{1}{r}\frac{\partial (r B_\theta)}{\partial r}. \tag{4.1}$$

For obvious geometrical reasons, this current profile (4.1) is different from the toroidal one. The advantage of using this current profile in the RMHD cylindrical code is that $q = q_{\mathrm{tor}}$ and hence resonances $q = m/n$ are at the same position with respect to plasma parameters profiles. The drawback of this option is, however, that the new current profile (4.1) has larger gradients at the edge and even can be negative to fit highly sheared profile $q = q_{\mathrm{tor}}$. This current in principle could be more 'tearing unstable' because of larger gradients [39]. However, in the present case the $n = 2$ mode was stable. Magnetic topology with the rotating plasma response at $\eta_0 = 10^{-8}$ and $t = 7 \times 10^3 \tau_A$, including diamagnetic effects and realistic neoclassical coefficients [28], is presented in figure 22. Note the strong screening of all harmonics on JET compared with the vacuum case. The perpendicular velocity (figure 23) at corresponding $r = r_{\mathrm{res}}$ is not zero for all harmonics, explaining the strong screening of RMPs, limiting the RMP penetration to the very edge. For JET plasma parameter profiles we did not find the situation of single island penetration on the top of the pedestal for DIII-D parameters (figures 11 and 17) where perpendicular electron velocity ($V_{E,\theta} + V^*_{\mathrm{e},\theta}$) is close to zero. The edge harmonic $m = 8$ penetrates because of higher resistivity as can be concluded from the screening factors profiles for harmonics ($n = -2$, $m = 3$–8) presented in figure 24.

5. RMP penetration on ITER

Finally let us consider ITER-like parameters: $R_M = 6.2\,\mathrm{m}$, $a = 2\,\mathrm{m}$, $B_\varphi \sim B_\mathrm{T} = 5.3\,\mathrm{T}$. Plasma profiles for standard H-mode scenario presented in figure 25, toroidal rotation $\Omega_{\varphi,0} = 6.2\,\mathrm{krad\,s^{-1}}$ and diamagnetic term parameter is $\delta = 0.009$ and central resistivity is taken $\eta_0 = 10^{-8}$. The corresponding neoclassical coefficients are presented in figure 26. The neoclassical poloidal viscosity is smaller for ITER compared with JET (figure 19) and DIII-D (figure 15) which is typically going to the lower collisionality plasmas. Vacuum modelling in torus for the latest design of ITER in-vessel RMP coils was done with the code ERGOS [9]. The three rows poloidally in each of the nine sectors are shown in sketch 27(*a*). Here coil coordinates (R, Z, ϕ) are approximated as follows. Top coil coordinates are upper conductor $R1 = 7.735\,\mathrm{m}$, $Z1 = 3.380\,\mathrm{m}$, lower conductor $R2 = 8.262\,\mathrm{m}$, $Z2 = 2.626\,\mathrm{m}$,

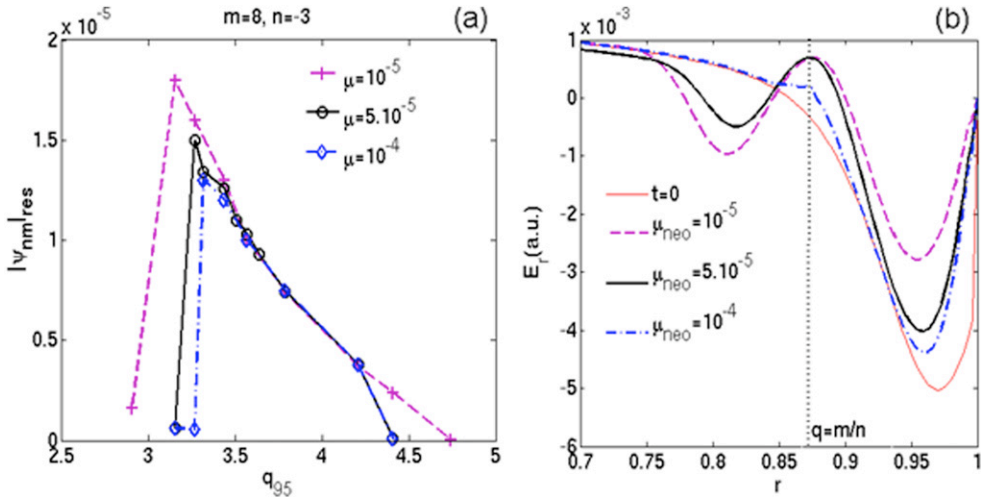

Figure 10. (*a*) Absolute value of the magnetic flux perturbation harmonic amplitude on the resonant surface at $t = 10^5\tau_A$ as a function of q_{95} for different neoclassical viscosity constant coefficients $\mu = \mu_{neo,1,2} = \text{const}$. (*b*) Stationary profiles of the radial electric field for different neoclassical viscosity constants used in modelling.

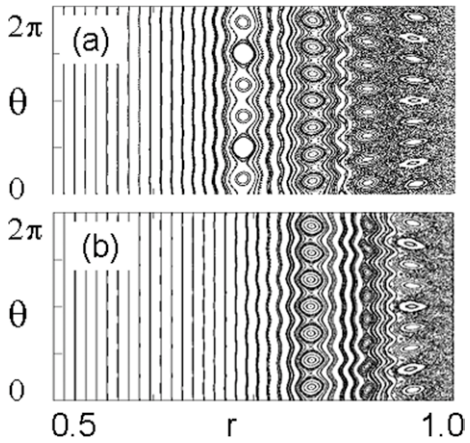

Figure 11. (*a*) Vacuum magnetic topology with RMP spectrum for DIII-D-like parameters. (*b*) The same as (*a*) but with neoclassical and diamagnetic effects at $t = 6 \times 10^4\tau_A$; $q_{95} = 3.15$.

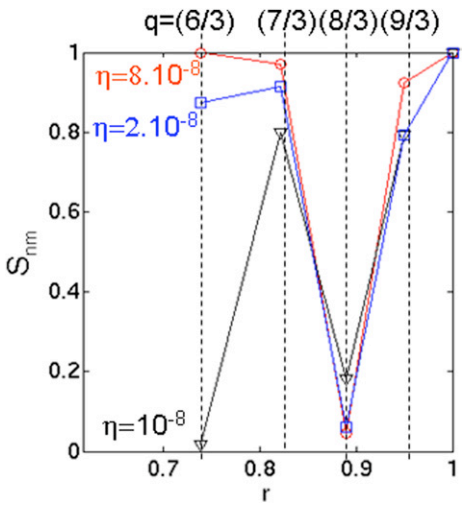

Figure 12. Screening factor ($S_{nm} = |\psi^{pl}_{nm}|/|\psi^{vac}_{nm}|$) profile for RMP spectrum in the resistivity scan at $t = 6 \times 10^4\tau_A$; $q_{95} = 3.15$.

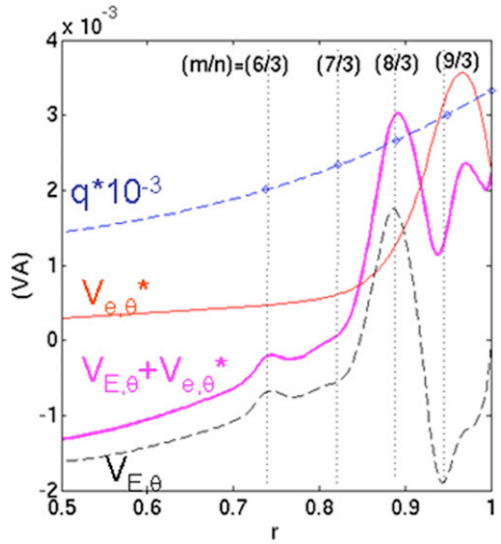

Figure 13. Components of the perpendicular velocity for DIII-D-like parameters and RMP spectrum $\psi_{n=-3;m=6,7,\ldots,10}(1) = (8, 7, \ldots, 4) \times 10^{-5}$ with neoclassical and diamagnetic effects at $t = 6 \times 10^4\tau_A$; $q_{95} = 3.15$. Here $V_{E,\theta}$ (dashed–dotted line); electron diamagnetic $V^*_{e,\theta}$ (thin); the sum $(V_{E,\theta} + V^*_{e,\theta})$ (bold), $q \cdot 10^{-3}$ profile (dashed). The positions of resonances are indicated by vertical lines.

$\phi_{centre} = 30°$, coil width in the toroidal direction $\Delta\phi_{coil} = 30°$, $\Delta\phi_{centre-centre} = 40°$. Mid-plane coil coordinates are upper conductor $-R1 = 8.618\,m$, $Z1 = 1.790\,m$, lower conductor $-R2 = 8.661\,m$, $Z2 = -0.550\,m$, $\phi_{centre} = 26.7°$, mid-coil width in the toroidal direction $\Delta\phi_{coil} = 20°$, $\Delta\phi_{centre-centre} = 40°$. Lower coil coordinates are upper conductor -$R1$ = 8.230 m, $Z1 = -1.546\,m$, lower conductor $-R2 = 7.771\,m$, $Z2 = -2.381\,m$, $\phi_{centre} = 30°$, coil width in the toroidal direction $\Delta\phi_{coil} = 30°$, $\Delta\phi_{centre-centre} = 40°$. The dc currents in the coils are distributed in a way to generate mainly $n = 3$ toroidal symmetry (in upper coils in [A]: 23220. −86940. 63630. 23310. −86940. 63630. 23310. −86940. 63630; in mid-plane coils: 0. 77940. −77940. 0. 77940.

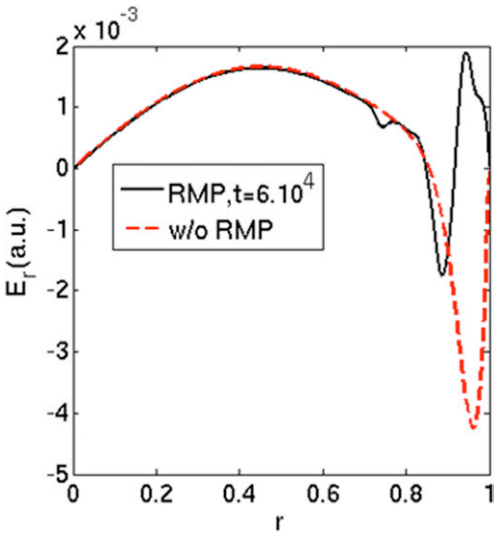

Figure 14. Radial electric field profile for DIII-D-like parameters and RMP spectrum $\psi_{n=-3;m=6,7,\ldots,10}(1) = (8, 7, \ldots, 4) \times 10^{-5}$ with neoclassical and diamagnetic effects at $t = 6 \times 10^4 \tau_A$; $q_{95} = 3.15$. The case without RMP (or at $t = 0$) is indicated by the dashed line.

-77940. 0. 77940. -77940; in lower coils: -27810. -60210. 88020. -27810. -60210. 88020. -27810. -60210. 88020). The corresponding profiles of magnetic flux perturbation harmonics ($n = -3, m = 4$–11), used for boundary conditions in the RMHD code: $\psi_{n=-3;m=4,..11}(1) = (6.89;\ 6.66;\ 6.31,\ 5.97;\ 5.64;\ 5.35;\ 4.98;\ 4.52) \times 10^{-5}$, are presented in figure 27(*b*). As discussed already in section 4, the main difficulty of toroidal q-profile approximation in the cylindrical code consists in the choice between cylindrical and toroidal q-profile since both options have their disadvantages and advantages, but neither can correctly reproduce toroidal geometry. Here we tried two options with the cylindrical q-profile matching the toroidal one in the centre and at the boundary and toroidal q-profiles (figure 28). One can see that the resonances at the same m-poloidal number move deeper towards the plasma centre if $q = q_{cyl} \neq q_{tor}$. Vacuum and with plasma response Poincaré plots for $q = q_{cyl} \neq q_{tor}$ are presented in figure 29. Only $m = 11$, $n = -3$ island chain forms on the $q = 11/3$ surface, but other harmonics are strongly screened. For $q = q_{tor}$ (figure 30), $q = m/n$ resonances have the same position compared with the torus, i.e. closer to the edge. In figure 31 one can see that the predictions for RMP screening factors for $n = -3$, m harmonics in ITER are different depending on the choice ($q = q_{cyl} \neq q_{tor}$ or $q = q_{tor}$), since corresponding positions of r_{res} and hence RMP amplitudes are different (larger towards the edge). In particular, $q = q_{tor}$ gives more optimistic predictions for RMP penetration in ITER. The screening factor is larger than one in the case of the so-called 'amplification' [5], which is seen, for example, for $m = 11$ and $m = 8$ harmonics in figure 31. Perpendicular (or here 'poloidal') velocity profiles under stationary conditions after $t = 10^4 \tau_A$ are presented in figure 32 for two approximations: (*a*) $q = q_{cyl} \neq q_{tor}$ and (*b*) $q = q_{tor}$. Note that due to RMP penetration, perpendicular velocity is decreased almost to zero only in the narrow region near $q = (11/3)$ for the (a) case and in much larger region near $q = (7/3) - (11/3)$ for the option (b). In case $q = q_{tor}$, RMP harmonics amplitudes are larger on the resonant surfaces, since resonances are closer to the edge. Even within limitations of the cylindrical code RMHD mentioned above, plasma response modelling indicated already that RMPs in plasma could be different compared with vacuum modelling. It is illustrated even more clearly in the following example of modelling for ITER. Here we used maximum possible current in each coil 90 kAt with π-phase shift between coils in the toroidal direction. Upper and lower coils in each of the nine sectors have the same sign of current and mid-plane coil has the opposite signs compared with upper and lower coils [40]. Vacuum modelling [40] predicted strong ergodization in the larger edge region in this case compared with the $n = 3$ case discussed above. The main toroidal number with these currents in RMP coils is $n = 4$, but side harmonics amplitudes $n = 1$, 2, 3, 5 are large. As a result, overlapping of islands is increased [40]. The boundary conditions for the RMP spectrum (here we used $n = 1:4$ and corresponding to them the main resonant m-harmonics) for the RMHD code were obtained using the ERGOS code [9]:

$$\psi_{n=-1;m=1-4}(1) = (2.5;\ 1.4;\ 1.1;\ 0.9) \times 10^{-5}$$

$$\psi_{n=-2;m=2-7}(1) = (1.;\ 0.9;\ 0.8;\ 0.7;\ 0.7;\ 0.68) \times 10^{-5}, \quad (5.1)$$

$$\psi_{n=-3;m=6-11}(1) = (1.34;\ 1.28;\ 1.22;\ 1.17;\ 1.13;\ 1.07) \times 10^{-5},$$

$$\psi_{n=-4;m=4-12}(1) = (4.56;\ 4.38;\ 4.18;\ 4.01;\ 3.77;\ 3.61;\ 3.41;\ 3.28;\ 3.08) \times 10^{-5}.$$

Here the toroidal q-profile $q = q_{tor}$ was used. Note the strong screening of all harmonics for this case (except the very edge ones) seen in figure 33, leading to the conclusion that vacuum predictions of plasma edge ergodization by RMPs are totally irrelevant in this case.

6. Conclusions and discussion

The non-linear reduced four-field RMHD model in cylindrical geometry with plasma rotation, neoclassical poloidal viscosity and two fluid diamagnetic effects was applied to the problem of RMP interaction with the rotating plasma. Due to the steep pressure gradients in the pedestal region, the components of flows perpendicular to the magnetic field, including $\vec{E} \times \vec{B}$ and electron diamagnetic rotation, play an essential role in RMP screening by plasma. Current perturbations generated in the narrow region (few mm) near rational surface $q = -m/n$ is the underlying physics of corresponding RMP harmonic (n, m) screening. The screening effect increases for lower resistivity, stronger rotation and smaller RMP amplitude. Typically RMP penetration occurs in the narrow region near the separatrix due to higher resistivity. However, at certain plasma parameters or/and because of the non-linear evolution of the radial electric field due to RMPs, $\vec{E} \times \vec{B}$ perpendicular rotation can be compensated by the electron diamagnetic rotation, i.e. $(V_{\theta,E\times B} + V^*_{\theta,e}) \sim 0$. In this case RMP harmonic (n, m) penetrates locally and forms islands on the corresponding resonance surface $q = m/n$.

For DIII-D-like parameters and RMPs with $n = -3$ toroidal number, islands are mainly screened in the plasma

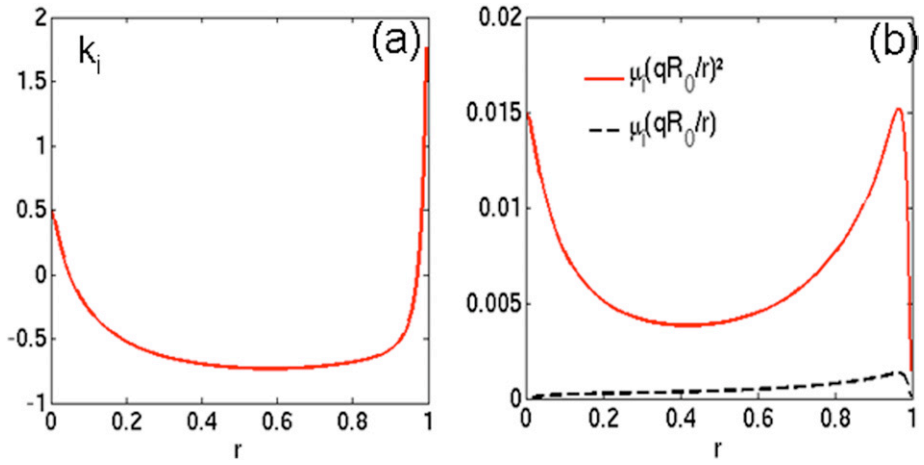

Figure 15. Neoclassical coefficients for DIII-D-like parameters presented in figure 1, $R_M = 1.8\,\mathrm{m}$, $a = 0.6\,\mathrm{m}$; $B_0 = 1.9\,\mathrm{T}$, cylindrical $q_{95} \sim 3.15$. (*a*) Profile of k_i, (*b*) profiles of $\mu_i(qR_0/r)^2$; $\mu_i(qR_0/r)$.

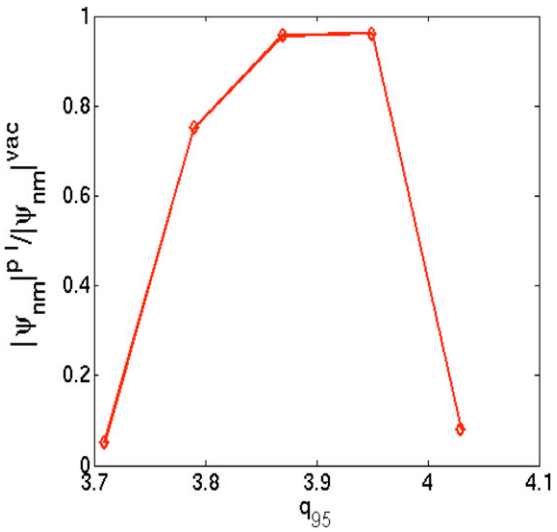

Figure 16. Screening factor ($S_{nm} = |\psi_{nm}^{\mathrm{pl}}|/|\psi_{nm}^{\mathrm{vac}}|$) on the resonant surface $q = 8/3$ in q_{95} scan for a single harmonic ($m = 8$, $n = -3$) with edge amplitude $\psi_{nm}(1) \sim 5 \times 10^{-5}$, $\eta_0 = 10^{-8}$, with realistic neoclassical coefficients (presented in figure 15) [28].

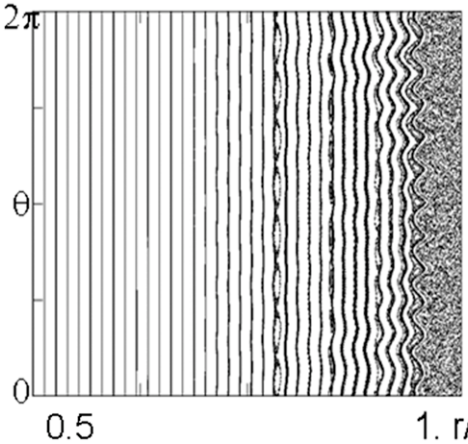

Figure 17. Magnetic topology in the case of RMP spectrum $\psi_{n=-3;m=6,7,\ldots,12}(1) = 5 \times 10^{-5}$ at $\eta_0 = 10^{-8}$, $q_{95} = 3.87$ with realistic neoclassical coefficients (presented in figure 15) [28]. Note penetration of the (8/3) island and very edge harmonics $m = 10$–12.

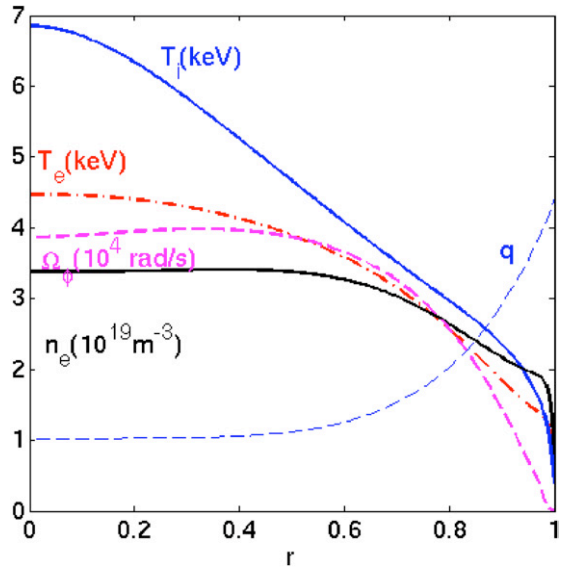

Figure 18. JET parameters (pulse #77329) used in modelling.

core and the ergodic zone is much narrower ($r_{\mathrm{erg}} > 0.95$) compared with vacuum modelling ($r_{\mathrm{erg}} > 0.9$). Depending on the q-profile, islands (7/3), (8/3) can penetrate if condition $(V_{\theta,E\times B} + V^*_{\theta,\mathrm{e}}) \sim 0$ is satisfied on the corresponding resonant surfaces. The q_{95} scan performed for ($n = -3$, $m = 8$) harmonic demonstrated rather narrow $\Delta q_{95} \sim 0.3$ penetration window for the island (8/3), situated approximately on the pedestal top.

For realistic JET parameters (shot #77329) and EFCC coils at $n = 2$, $I_{\mathrm{EFCC}} = 40\,\mathrm{kAt}$, a strong RMP screening was observed in modelling except for the very edge ($r > 0.98$). Compared with DIII-D parameters in the JET case we did not find the situation where the perpendicular electron velocity $(V_{E,\theta} + V^*_{\mathrm{e},\theta})$ is close to zero on the pedestal top providing RMP penetration in this region.

ITER standard H-mode scenario and RMP in-vessel coil parameters were used in modelling. For the case $n = -3$, $m = 4:11$ spectrum and $q = q_{\mathrm{cyl}} \neq q_{\mathrm{tor}}$, strong screening of all harmonics except for $m = 11$ was demonstrated. In contrast for more realistic positions of resonances at $q = q_{\mathrm{tor}}$ edge

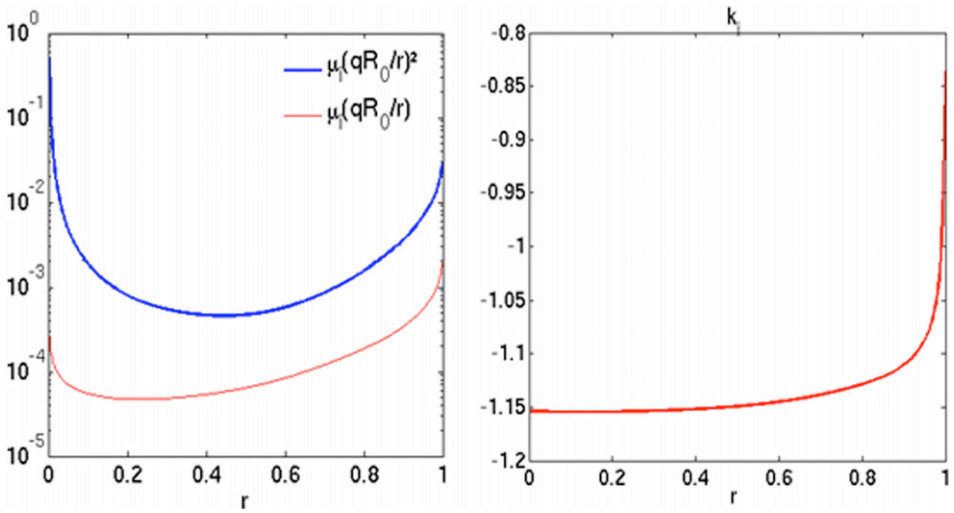

Figure 19. Corresponding to JET shot #77329 parameters normalized neoclassical poloidal viscosity (right) and k_i (left) coefficients.

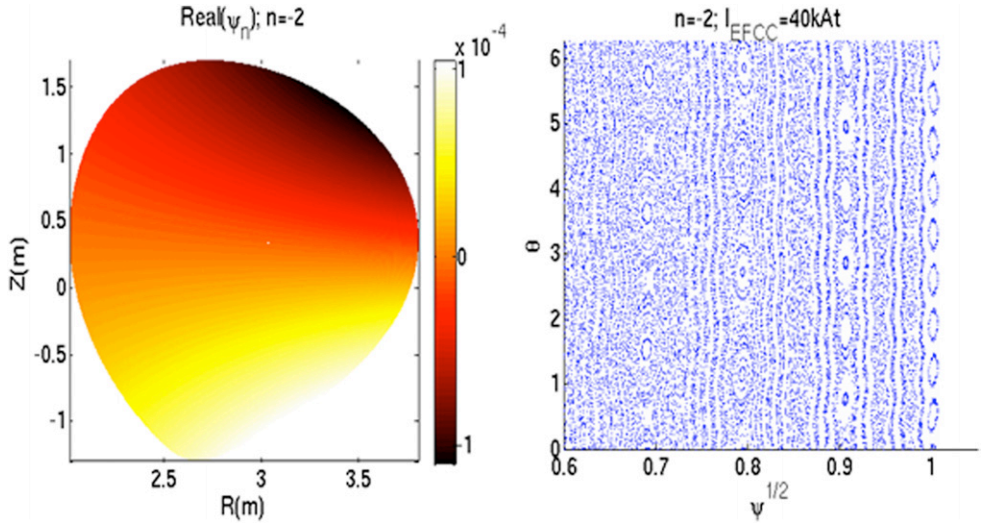

Figure 20. Vacuum modelling in torus with the code ERGOS [9]. (*a*) Normalized Real$(\psi_n)|_{\varphi=0}$, (*b*) Poincaré plot in magnetic flux coordinates $\{\sqrt{\psi};\theta;\varphi=0\}$ in vacuum ($I_{\mathrm{EFCC}}=40\,\mathrm{kAt}$, $n=-2$).

harmonics $m=7:11$ can penetrate and form an ergodic region in ITER. Perpendicular (or here 'poloidal') plasma velocity is strongly modified by RMP and is close to zero in this case $(V_{E,\theta}+V^*_{\mathrm{e},\theta})\sim 0$, which is favourable for RMP penetration. In the case of $n=1:4$ spectrum and maximum current 90 kAt in each coil strong screening of RMPs is observed limiting the ergodic region to the very edge. With this respect the $n=-3$ option remains more favourable for ITER.

The cylindrical RMHD code results presented here are obviously limited in exact predictions of RMPs screening in ITER. Note, however, the generic feature of RMP interaction with rotating plasma: higher RMP amplitudes, higher resistivity, lower rotation, lower neoclassical poloidal viscosity are favourable factors for RMP penetration. ELM suppression physics with respect to screening of RMPs was not treated in the paper and still remains an open question. The next step in understanding RMP penetration in ITER should be based on the non-linear MHD code JOREK in realistic toroidal geometry [14]. This study is under way at present and will be presented in a dedicated paper.

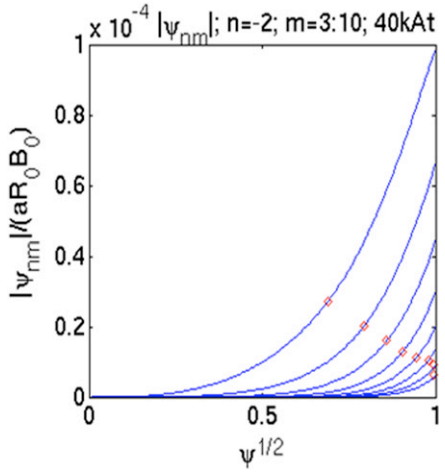

Figure 21. Normalized harmonics ($n=-2$, $m=3:10$) amplitude profiles in vacuum resulting from the ERGOS code for $I_{\mathrm{EFCC}}=40\,\mathrm{kAt}$. Edge values were used as input for the RMHD code in the JET case.

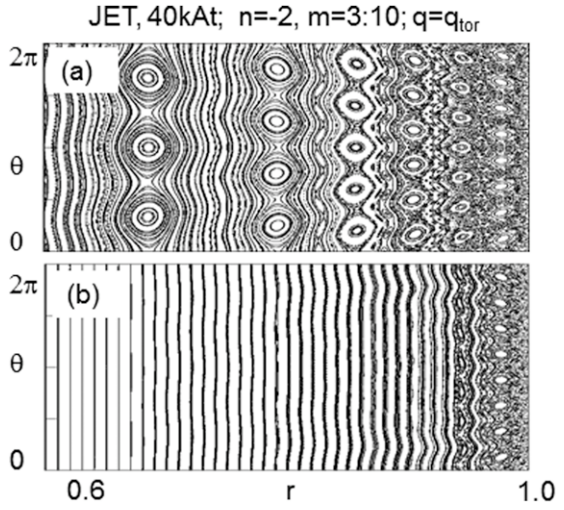

Figure 22. Magnetic topology resulting from the cylindrical code RMHD for the JET case at $I_{\mathrm{EFCC}} = 40\,\mathrm{kAt}$, $n = -2$. (*a*) Vacuum ($\eta_0 = 10^{-2}$) without rotation, (*b*) with rotating plasma response at $t = 7 \times 10^3 \tau_{\mathrm{A}}$, $q = q_{\mathrm{tor}}$.

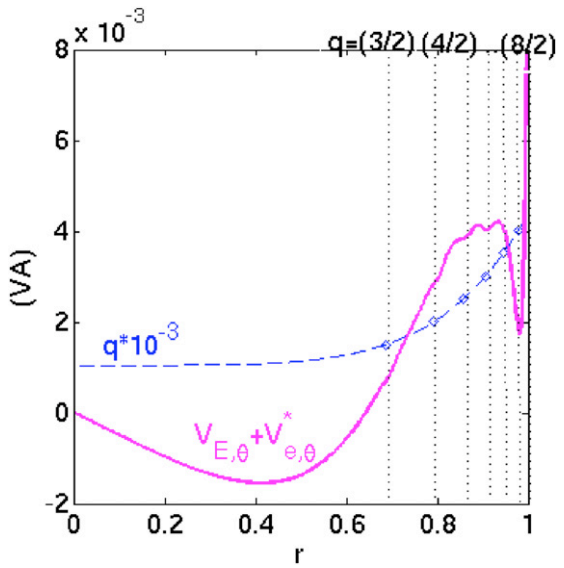

Figure 23. Poloidal components of the perpendicular velocity for JET parameters at $I_{\mathrm{EFCC}} = 40\,\mathrm{kAt}$, $n = -2$, $m = 3$–8 with neoclassical and diamagnetic effects at $t = 6 \times 10^3 \tau_{\mathrm{A}}$; $q = q_{\mathrm{tor}}$. Here, perpendicular electron velocity profile ($V_{E,\theta} + V^*_{e,\theta}$) is in bold, the $q \cdot 10^{-3}$ profile is shown by the dashed line with diamonds indicating resonance surfaces $q = (3/2)$; $(4/2)$, etc).

Appendix

In the following we present the derivation of neoclassical terms (2.5)–(2.6) we added to the model (2.1)–(2.4) in section 2. In the four-fluid model [24–26] usually the fluid velocities for species s (s = e,i- is for electron and ions) are approximated as

$$\vec{V}_s \approx \vec{V}_E + \vec{V}_{||,s} + \vec{V}^*_s \qquad \text{(A.1)}$$

where

$$\vec{V}_{\|,s} = \frac{1}{B^2}(\vec{V}_s\vec{B})\vec{B} = V_s\vec{b}; \qquad \vec{V}_E = \frac{\vec{E}\times\vec{B}}{B^2};$$

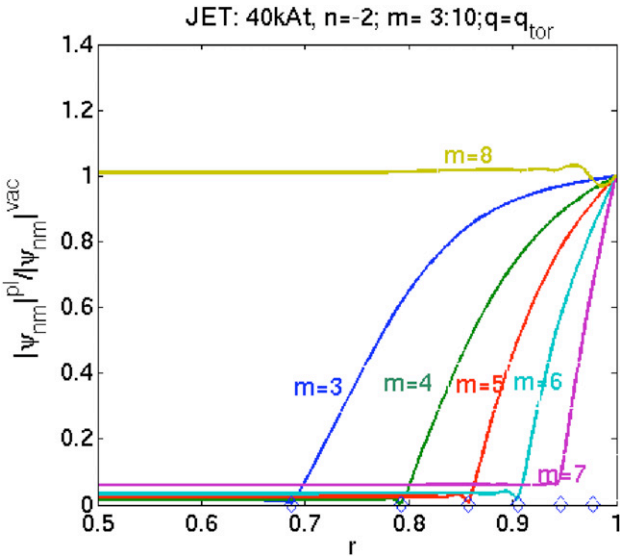

Figure 24. Screening factor ($S_{nm} = |\psi^{\mathrm{pl}}_{nm}|/|\psi^{\mathrm{vac}}_{nm}|$) profiles for JET parameters at $I_{\mathrm{EFCC}} = 40\,\mathrm{kAt}$, resonant harmonics $n = -2$, $m = 3 - -8$ with neoclassical and diamagnetic effects at $t = 7 \times 10^3 \tau_{\mathrm{A}}$; $\eta_0 = 10^{-8}$, $q = q_{\mathrm{tor}}$.

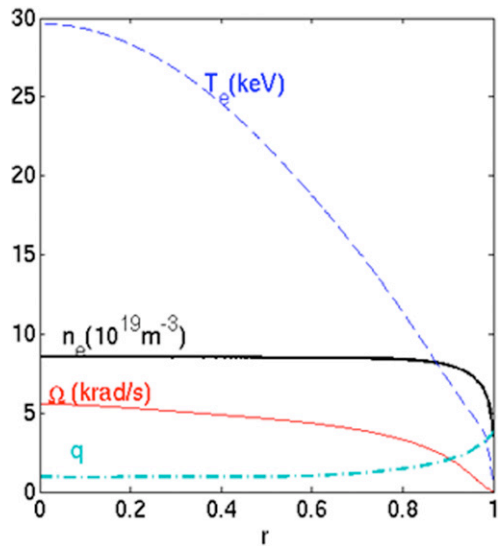

Figure 25. ITER H-mode scenario parameters used in modelling.

$$\vec{V}^*_s = \frac{\vec{B}\times\nabla p_s}{e_s n_s B^2}.$$

Generally in the RMHD model the 'perpendicular' to the magnetic field flows are approximated as follows:

$$\vec{V}_E = \frac{\vec{E}\times\vec{B}}{B^2} \approx -\frac{\nabla\Phi\times\vec{e}_\varphi}{B};$$

$$\vec{V}^*_s = \frac{\vec{B}\times\nabla p_s}{e_s n_s B^2} \approx -\frac{\nabla p_s\times\vec{e}_\varphi}{n_s m_s \Omega_{cs}},$$

using the fact that the toroidal magnetic field is much larger than the poloidal one. Hence, in the equilibrium 'perpendicular' to the magnetic field mean flow is 'poloidal'. At large aspect ratio assumption (cylindrical code RMHD) $\vec{e}_\varphi \approx \vec{e}_z$ and θ corresponds to the geometrical poloidal angle. However, it is not the case in the realistic toroidal

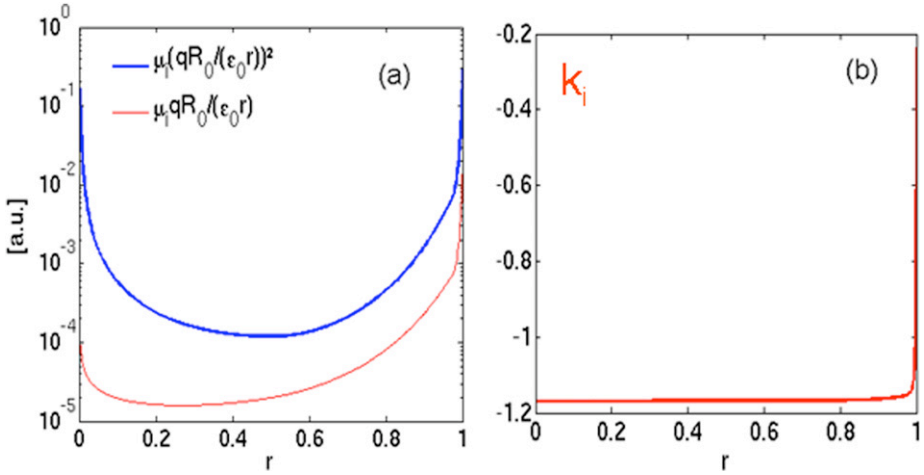

Figure 26. Neoclassical coefficients corresponding to ITER parameters presented in figure 25.

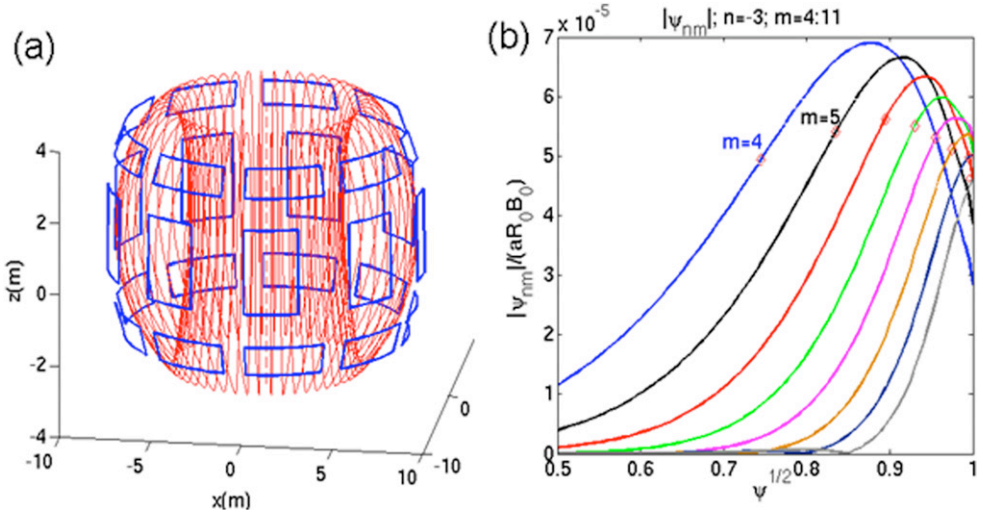

Figure 27. (*a*) ITER RMP coils representation in the ERGOS vacuum code in the toroidal geometry; (*b*) magnetic flux perturbation profiles for $n = 3$, $m = 4:11$ harmonics.

geometry, where the term 'poloidal' (θ) direction is defined as tangential to the magnetic flux surface with unit vector: $\vec{e}_\theta = R/|\vec{\nabla}\psi|(\vec{\nabla}\varphi \times \vec{\nabla}\psi)$. To avoid any misunderstanding in the following discussion we use mainly the term 'perpendicular' velocity, which is the main factor in RMP screening [22].

Similar to [24] the equation of motion for species (s) was used in the form

$$m_s n_s \left[\frac{\partial(\vec{V}_E + \vec{V}_{\parallel,s} + \vec{V}_{p_s})}{\partial t} + (\vec{V}_E + \vec{V}_{\parallel,s} + \vec{V}_s^*) \cdot \nabla(\vec{V}_E + \vec{V}_{\parallel,s} + \vec{V}_s^*) \right] + \nabla \cdot \boldsymbol{P}_s - e_s n_s(\vec{E} + \vec{V}_s \times \vec{B}) = \vec{F}_s. \quad \text{(A.2)}$$

The pressure tensor can be represented as $\boldsymbol{P}_s = \boldsymbol{I} p_s + \Pi_s$, where p_s is a scalar pressure for species and viscous tensor can be represented in two parts: gyroviscosity and neoclassical parallel viscosity: $\Pi_s = \Pi_s^{\mathrm{g}} + \Pi_s^{\mathrm{neo}}$. The explicit form of Π_s^g is usually not needed in reduced MHD because of gyroviscous cancellation [24]. For the neoclassical part of the pressure

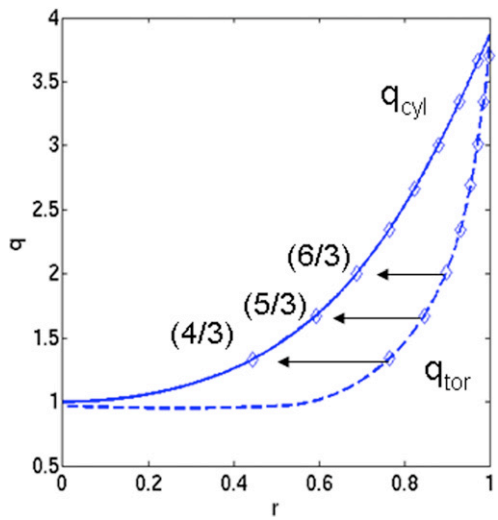

Figure 28. q-profiles used in RMHD modelling for ITER.

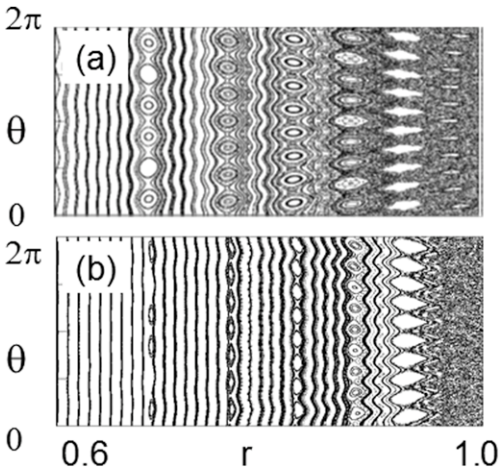

Figure 29. Magnetic topology in ITER due to RMP coils at $n = -3$ with cylindrical q-profile: $q = q_{\rm cyl} \neq q_{\rm tor}$ in vacuum-(a), in plasma-(b).

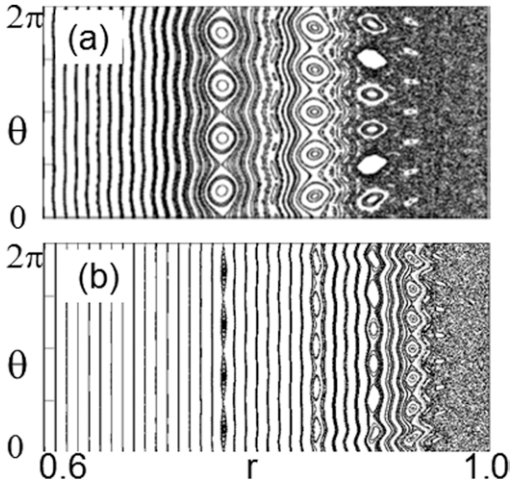

Figure 30. Magnetic topology in ITER due to RMP coils at $n = -3$ with toroidal q-profile: $q = q_{\rm tor}$ in vacuum (a) and in plasma (b).

tensor here we used the simplified heuristic closure from [27]:

$$\nabla \cdot \Pi_s^{\rm neo} \approx n_s m_s \mu_s \frac{B^2}{B_\theta^2}(\vec{V}_s \vec{e}_\theta + k_s \vec{V}_{T,s} \vec{e}_\theta)\vec{e}_\theta \qquad (A.3)$$

where

$$\vec{V}_{T,s} = \frac{\vec{B} \times \nabla T_s}{e_s B^2} \approx -\frac{\nabla T_s \times \vec{e}_z}{m_s \Omega_{cs}} + O(\varepsilon),$$

the expressions of the neoclassical poloidal flow damping rate and coefficient k_s are given in [27, 28]. The electron part of the neoclassical pressure tensor enters in Ohm's law and describes the bootstrap current [28, 37]. The bootstrap current evolution is not treated in this work and is considered to be a part of the total equilibrium parallel current profile given at the beginning of the modelling at $t = 0$. Hence the equation of motion for ions is represented in the form

$$m_{\rm i} n_{\rm e} \left[\left(\frac{\partial}{\partial t} + \vec{V}_i \cdot \nabla\right)\vec{V}_E + \left(\frac{\partial}{\partial t} + \vec{V}_E \cdot \nabla\right)\vec{V}_{||,{\rm i}} + (\vec{V}_{||,{\rm i}} \nabla)\vec{V}_{||,{\rm i}}\right] + \nabla P + m_{\rm i} n_{\rm e} \mu_{\rm i} \frac{B^2}{B_\theta^2}(V_{\theta,{\rm i}} + k_{\rm i} V_{\theta,T_{\rm i}})\vec{e}_\theta = \vec{J} \times \vec{B}. \qquad (A.4)$$

Note that in cylindrical approximation we used the expression

$$V_{\theta,{\rm i}} + k_{\rm i} V_{\theta,T_{\rm i}} = \frac{1}{B}\frac{\partial \Phi}{\partial r} + V\frac{r}{qR_0} + \frac{1}{m_{\rm i} n_{\rm e} \Omega_{\rm ci}}\frac{\partial (T_{\rm i} n_{\rm e})}{\partial r} + k_{\rm i}\frac{1}{m_{\rm i}\Omega_{\rm ci}}\frac{\partial T_{\rm i}}{\partial r}.$$

The parallel momentum equation is obtained from the scalar product of (A.3) with unit vector $\vec{b}$ parallel to the total magnetic field:

$$\vec{b}\left(m_{\rm i} n_{\rm e}\left[\left(\frac{\partial}{\partial t} + \vec{V}_E \cdot \nabla\right) V\vec{b} + \vec{b} V \nabla_\parallel V\right] + \vec{\nabla} P + m_{\rm i} n_{\rm e} \mu_{\rm i} \frac{1}{b_\theta^2} \times \left(\frac{1}{B}\frac{\partial \Phi}{\partial r} + V\frac{r}{qR_0} + \frac{1}{m_{\rm i} n_{\rm e}\Omega_{\rm ci}}\frac{\partial (T_{\rm i} n_{\rm e})}{\partial r} + k_{\rm i}\frac{1}{m_{\rm i}\Omega_{\rm ci}}\frac{\partial T_{\rm i}}{\partial r}\right)\vec{e}_\theta\right) = 0. \qquad (A.5)$$

From (A.5) it is easy to see that the additional term due to the neoclassical viscosity tensor has the form

$$F_\parallel^{\rm neo} = -\mu_{\rm i}\frac{qR_0}{r}\left(\frac{\partial \Phi}{\partial r} + V\frac{r}{qR_0} + \frac{\delta\tau}{n_{\rm e}}\frac{\partial p}{\partial r} + \tau\delta k_{\rm i}\frac{\partial T_{\rm e}(r)}{\partial r}\right). \qquad (A.6)$$

In the model (A.6) is taken into account only for the mean flow (harmonic $n = 0, m = 0$). Normalized neoclassical viscosity is $\mu_{\rm i} = \mu_{\rm i}^{\rm (ph)}\tau_{\rm A}$.

Vorticity equation with neoclassical parallel viscosity terms can be obtained by taking $\vec{e}_z \cdot \nabla\times$ of equation (A.4). The detailed derivation of the vorticity equation without neoclassical terms is given in the literature [24]. So we give here only the derivation of the additional 'neoclassical' term in the vorticity equation (2.2):

$$\begin{aligned} F_\perp^{\rm neo,(ph)} &= \vec{e}_z \cdot \nabla \times \left\{\mu_{\rm i}\frac{1}{b_\theta^2}(V_{\theta,{\rm i}} + k_{\rm i} V_{\theta,T_{\rm i}})\vec{e}_\theta\right\} \\ &= \mu_{\rm i}\frac{1}{b_\theta^2}\vec{e}_z \cdot \nabla \times \left(\frac{1}{B_T}\frac{\partial \Phi}{\partial r} + V\frac{r}{qR_0} + \frac{\tau}{m_{\rm i} n_{\rm e}\Omega_{\rm ci}}\frac{\partial (T_{\rm e} n_{\rm e})}{\partial r} + k_{\rm i}\frac{\tau}{m_{\rm i}\Omega_{\rm ci}}\frac{\partial T_{\rm e}}{\partial r}\right)\vec{e}_\theta \qquad (A.7) \\ &= \frac{\mu_{\rm i}}{b_\theta^2}\frac{1}{r}\left\{\frac{\partial}{\partial r}\left(r\left(\frac{1}{B_{\rm T}}\frac{\partial \Phi}{\partial r} + V\frac{r}{qR_0} + \frac{\tau}{m_{\rm i} n_{\rm e}\Omega_{\rm ci}}\frac{\partial (T_{\rm e} n_{\rm e})}{\partial r} + k_{\rm i}\frac{\tau}{m_{\rm i}\Omega_{\rm ci}}\frac{\partial T_{\rm e}}{\partial r}\right)\right)\right\}. \end{aligned}$$

Here we assumed that $\partial/\partial r(r(\mu_{\rm i}/b_\theta^2))$ is small compared with other terms, which was verified numerically using for $\mu_{\rm i}$ the expressions from [28].

The normalized neoclassical term in (2.2) is used only for the mean poloidal flow:

$$F_\perp^{\rm neo} = -\mu_{\rm i}\left(\frac{qR_0}{r}\right)^2 \times \left\{W - \frac{1}{r}\frac{\partial}{\partial r}\left(r\left(V\frac{r}{qR_0} + \frac{\tau\delta}{n_{\rm e}}\frac{\partial p}{\partial r} + k_{\rm i}\tau\delta\frac{\partial T_{\rm e}}{\partial r}\right)\right)\right\}. \qquad (A.8)$$

The use of closer (A.2) results in the fact that due to the large neoclassical poloidal viscosity poloidal rotation without RMPs tends to the neoclassical value proportional to the ion temperature gradient due to the large neoclassical poloidal viscosity [27, 28]:

$$V_\theta \to V_\theta^{\rm neo} \approx -\frac{k_{\rm i}}{m_{\rm i}\Omega_{\rm ci}}\frac{\partial T_{\rm i}}{\partial r}. \qquad (A.9)$$

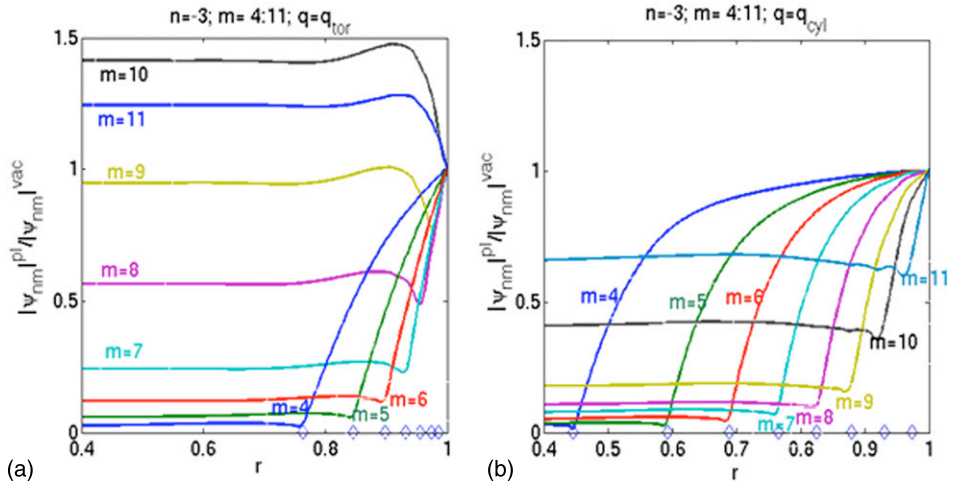

Figure 31. Screening factor for different poloidal harmonics m at $n = -3$ for $q = q_{\rm tor}$ (a), $q = q_{\rm cyl} \neq q_{\rm tor}$ (b).

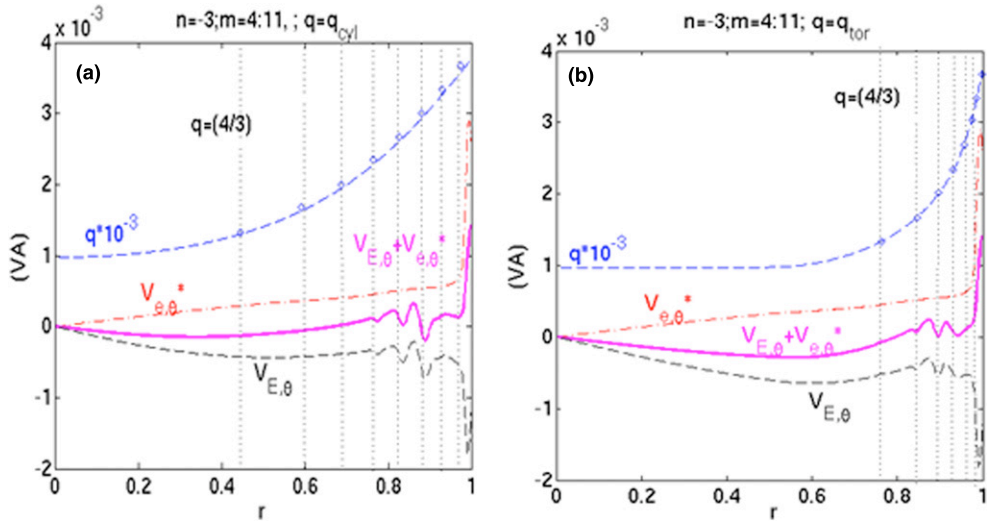

Figure 32. Components of the perpendicular velocity for $n = 3$ RMP spectrum for ITER parameters at $n = -3$ for (a) with $q = q_{\rm cyl} \neq q_{\rm tor}$, (b) with $q = q_{tor}$. Here, $V_{E,\theta}$(dashed); electron diamagnetic $V^*_{e,\theta}$ (dashed–dotted); the sum $(V_{E,\theta} + V^*_{e,\theta})$(bold), $q \cdot 10^{-3}$ profile (dashed with diamonds). The positions of resonances are indicated by vertical lines.

Certainly, we are aware of the limits of this approach, since at present the predictive capacity of neoclassical theory for poloidal rotation in tokamaks is rather limited. Usually poloidal rotation is measured for carbon impurities (C^{4+}, C^{6+}) by Doppler CXRS measurements [29, 30]. The information about poloidal rotation for the main species is not directly available in the experiment, since the impurity flows differ from the bulk ions for different reasons, demanding self-consistent modelling of flows in multi-species plasma [29], taking into account ionization and neutrals at the edge [31], plasma turbulence in the core, etc. [32, 33]. Note that at present the self-consistent predictive first-principles theory of poloidal rotation is still missing. The measured poloidal rotation was shown to deviate from neoclassical predictions especially in the plasma core [34] and in the presence of internal transport barriers [30]. Note also that drift-kinetic simulations [35, 36] pointed out the importance of the direct ion-orbit losses in the pedestal region leading to corrections to the neoclassical theory also in the pedestal. However, in the pedestal region in spite of the extensive debates [31, 35, 36], the order of magnitude and the form of poloidal velocity profile is closer to neoclassical predictions in many experimental cases [29]. This motivated us to include the poloidal viscosity tensor in MHD modelling using its neoclassical form as a first step approximation to capture main physics of interest here which is the change of the poloidal flow and the edge radial electric field due to RMPs in H-mode plasmas.

Acknowledgments

This work, supported by the European Communities under the contract of Association between EURATOM and CEA, was carried out within the framework of the European Fusion Development Agreement. The views and opinions expressed herein do not necessarily reflect those of the European Commission. Section 5 of the paper was supported within the framework of the Fusion for Energy grant *F4E-GRT-055* (*PMS-PE*). This work was also part-funded by the Grant Agency of the Czech Republic under grant P205/11/2341.

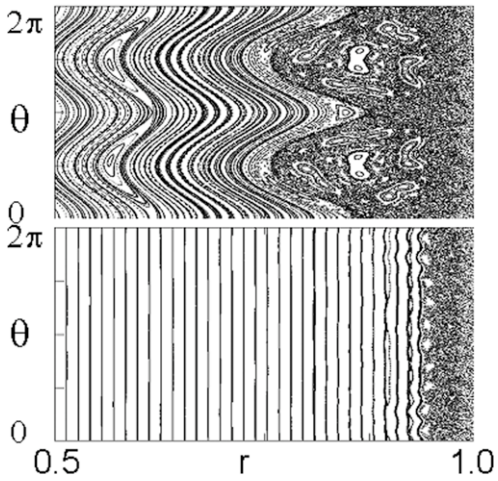

Figure 33. Poincaré plots for vacuum (top) and with plasma response (bottom) for RMP modelling in ITER for $n = 4, 3, 2, 1$ spectrum ($n = 4$ is the main harmonic) with maximum 90 kAt current in each coil.

References

[1] Loarte A. *et al* 2010 Fusion Energy *Proc. 23rd Int. Conf. Daejeon, 2010* (Vienna: IAEA) CD-ROM file ITR/1-4 and http://www-pub.iaea.org/mtcd/meetings/cn180_papers.asp
[2] Klimov N. *et al* 2009 *J. Nucl. Mater.* **390–391** 721
[3] Hawryluk R. *et al* 2009 *Nucl. Fusion* **49** 065012
[4] Evans T.E. *et al* 2008 *Nucl. Fusion* **48** 02400
[5] Burrell K. *et al* 2005 *Plasma Phys. Control. Fusion* **47** B37
[6] Suttrop W. *et al* 2011 *Phys. Rev. Lett.* **106** 225004
[7] Liang Y. *et al* 2007 *Phys. Rev. Lett.* **98** 265004
[8] Fenstermacher M. *et al* 2008 *Phys. Plasmas* **15** 56122
[9] Becoulet M. *et al* 2008 *Nucl. Fusion* **48** 024003
[10] Schaffer M. *et al* 2008 *Nucl. Fusion* **48** 024004
[11] Joseph I. *et al* 2008 *Nucl. Fusion* **48** 045009
[12] Canik J.M. *et al* 2010 *Nucl. Fusion* **50** 034012
[13] Kirk A. *et al* 2010 *Nucl. Fusion* **50** 034008
[14] Huysmans G.T.A. *et al* 2009 *Plasma Phys. Control. Fusion* **51** 124012
[15] Fitzpatrick R. 1998 *Phys. Plasmas* **5** 3325
[16] Heyn M.F. *et al* 2008 *Nucl. Fusion* **48** 024005
[17] Becoulet M. *et al* 2009 *Nucl Fusion* **49** 085011
[18] Kikuchi Y. *et al* 2006 *Plasma Phys. Control. Fusion* **48** 169
[19] Strauss H. *et al* 2009 *Nucl. Fusion* **49** 055025
[20] Izzo V.A. and Joseph I. 2008 *Nucl. Fusion* **48** 115004
[21] Nardon E. *et al* 2007 *Phys. Plasmas* **14** 092501
[22] Nardon E. *et al* 2010 *Nucl. Fusion* **50** 034002
[23] Reiser D. *et al* 2009 *Phys. Plasmas* **16** 042317
[24] Hazeltine R.D. 1985 *Phys. Fluids* **28** 2977
[25] Huysmans G. 2001 *Phys. Rev. Lett.* **87** 245002
[26] Aydemir A.Y. 1992 *Phys. Fluids* **64** 11 3469
[27] Gianakon T.A. *et al* 2002 *Phys. Plasmas* **9** 536–47
[28] Kessel C.E. 1994 *Nucl. Fusion* **34** 1221
[29] Field A.R. *et al* 2009 *Plasma Phys. Control. Fusion* **51** 105002
[30] Crombe K. *et al* 2005 *Phys. Rev. Lett.* **95** 155003
[31] Stacey W.M. 2008 *Phys. Plasmas* **15** 012501
[32] Waltz R.E. *et al* 2007 *Phys. Plasmas* **14** 122507
[33] Dif-Pradalier G. *et al* 2009 *Phys. Rev. Lett.* **103** 065002
[34] Solomon W. 2006 *Phys. Plasmas* **13** 056116
[35] Chang C.S. *et al* 2004 *Phys. Plasmas* **11** 2649
[36] Bell R.E. *et al* 2010 *Phys. Plasmas* **17** 082507
[37] Smolyakov A. 2004 *Phys. Plasmas* **11** 4353
[38] Waelbroeck F.L. 2003 *Phys. Plasmas* **10** 4040
[39] Hegna C.C. and Callen J.D. 1994 *Phys. Plasmas* **1** 2308
[40] Orlov D. *et al* 2010 Numerical analysis of resonant magnetic perturbations for ELM control in ITER, P.2.150 *Proc. 37th EPS Conf. (Dublin, Ireland, 2010)*